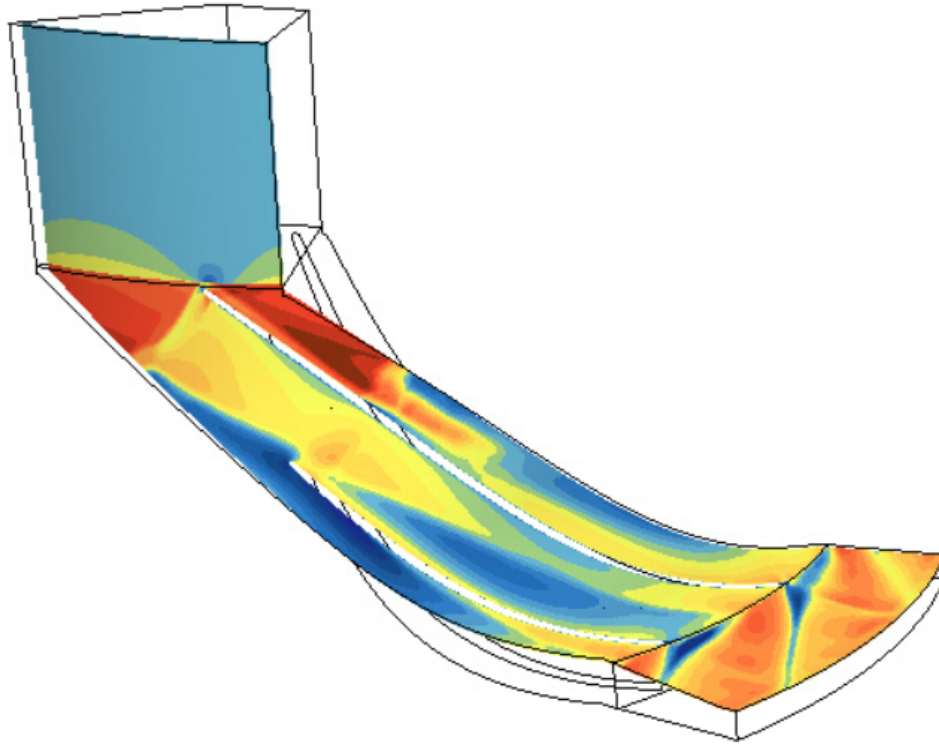




CHALMERS
UNIVERSITY OF TECHNOLOGY



Simcenter STAR-CCM+



CFD Simulation of a Centrifugal Compressor using Star-CCM+

Master's thesis in Applied Mechanics

SAI ANIRUDH RAVICHANDRAN

DEPARTMENT OF MECHANICS AND MARITIME SCIENCE

CHALMERS UNIVERSITY OF TECHNOLOGY
Göteborg, Sweden 2022
www.chalmers.se

MASTER'S THESIS 2022

CFD Simulation of a Centrifugal Compressor using Star-CCM+

SAI ANIRUDH RAVICHANDRAN



Department of Mechanics and Maritime Sciences
Division of Fluid Mechanics
CHALMERS UNIVERSITY OF TECHNOLOGY
Göteborg, Sweden 2022

CFD Simulation of a Centrifugal Compressor using Star-CCM+
SAI ANIRUDH RAVICHANDRAN

© SAI ANIRUDH RAVICHANDRAN, 2022.

Supervisor: Ranjan Saha, Siemens Energy AB

Examiner: Tomas Grönstedt, Department of Mechanics and Maritime Sciences

Master's Thesis 2022

Department of Mechanics and Maritime Sciences

Division of Fluid Dynamics

Chalmers University of Technology

SE-412 96 Göteborg

Telephone +46 31 772 1000

Cover: Contour plot of relative Mach number near the casing of the compressor at the design point outlet pressure.

Typeset in L^AT_EX

Printed by Chalmers Reproservice

Göteborg, Sweden 2022

Abstract

With anthropogenic greenhouse gas every year, its effect on the climate change is higher than ever and the need to curtail the emission of greenhouse gases is high. Decarbonization of district heat pumps is a step in the right direction to reduce the effects of such machines on climate change. In this case, the working fluid in the heat pump is replaced from R134a which has a GWP of 1430 to R1234ze(E) which has a GWP of 6.

The main aim of this work is to perform CFD simulations of a centrifugal compressor using Star-CCM+. The compressor is tested for different outlet pressure conditions to create a compressor map with in-depth analysis of the impact of various factors on the performance. The working fluid is R1234ze(E) which is a low GWP refrigerant. The results obtained from the simulations would then be compared with the in-house and ANSYS CFX results.

The process starts from acquiring the geometry and preparing it for meshing. The main task was to add the inlet part and the diffuser part to the compressor. The diffuser dimensions were provided which was added to the impeller. The final geometry is then meshed appropriately and the physics models required are added. The fluid and thermodynamic properties of the refrigerant are obtained from REFPROP and are added to the material database. With all the prerequisites set, simulations are performed. The outlet pressure is changed for every case and the important compressor characteristics are noted.

Properties of the flow are recorded at different boundaries and are used to evaluate the compressor performance using appropriate equations. The effect of different turbulence models and real gas equations are studied. Also, the effect of the diffuser on the compressor is studied by analysing the efficiency curve. The difference between the polytropic efficiency and the isentropic efficiency for a compressor is also observed as expected. Finally, the operation analysis at design point and off-design are performed by looking at the flow through the compressor at different spanwise locations.

Keywords: CFD, centrifugal compressor, isentropic efficiency, polytropic efficiency, pressure ratio.

Preface

The Master Thesis work is carried out from February 2022 to June 2022 with Siemens Energy at Finspång. The project is supervised by Ranjan Saha and Thomas Widgren from Siemens Energy and examined by Tomas Grönstedt at the Chalmers University of Technology.

Acknowledgements

I would like to express my sincere gratitude to Ranjan Saha and Thomas Widgren for their guidance and support throughout the project. Their technical knowledge and inputs provided about the compressor and the working fluid were pivotal for the completion of this work. They also conducted regular meetings and provided valuable feedback on my progress despite these unprecedented times that we are living in. Next I would like to thank my thesis partner Rahul Gudur Suresh for all the discussions regarding the CFD setup, the efficiency calculations and other interesting conversations. I would also like to thank my examiner Tomas Grönstedt for his valuable input and suggestions to make this work better.

Lastly, I would like to thank my family for always supporting me in all my decisions. Without their support I would not be here.

Sai Anirudh Ravichandran, Göteborg, June 2022

List of Acronyms

Below is the list of acronyms that have been used throughout this thesis listed in alphabetical order:

CFC	Chlorofluorocarbons
CFD	Computational Fluid Dynamics
COP	Coefficient Of Performance
FEA	Finite Element Analysis
GHG	GreenHouse Gases
GWP	Global Warming Potential
HCFC	Hydrochlorofluorocarbons
HFC	Hydrofluorocarbons
IGV	Inlet Guide Vanes
LE	Leading Edge
NIST	National Institute of Standards and Technology
REFPROP	Reference Fluid Thermodynamic and Transport Properties Database
TE	Trailing Edge

Nomenclature

Below is the nomenclature of indices, sets, parameters, and variables that have been used throughout this thesis.

Indices

01	Stagnation value at inlet
02	Stagnation value at outlet
CV	Control volume
i	Inlet
in	Inlet
is	Isentropic
o	Outlet
out	Outlet
x	Direction of application of force
θ	Tangential component

Parameters

η_{tt}	Total to total isentropic efficiency
η_p	Polytropic efficiency
τ_A	Rate of change of angular momentum
U	Tip speed

Variables

α	attractive term in the original Redlich-Kwong equation
γ	Ratio of specific heats
c_p	Specific heat at constant p

κ	Isentropic coefficient
P_c	Pressure at critical point
P_r	Reduced pressure
r	Distance from the mass center of the axis of rotation
R	Universal gas constant
T_c	Temperature at critical point
T_r	Reduced temperature
v	Specific volume
\dot{W}_c	Specific work
ω	Accentric factor

Contents

List of Acronyms	ix
Nomenclature	xi
List of Figures	xv
List of Tables	xix
1 Introduction	1
1.1 Aim	2
1.2 Tools Used	2
1.3 Limitations	2
2 Theory	3
2.1 Heat pump	3
2.1.1 Domestic heat pumps	3
2.1.1.1 Air source heat pump	4
2.1.1.2 Ground source heat pump	4
2.1.1.3 Water source heat pump	5
2.1.2 Industrial scale heat pumps	6
2.2 Centrifugal compressor	6
2.3 Components of a centrifugal compressor	7
2.4 Compressor Performance	8
2.4.1 Work	8
2.4.1.1 Newton's second law of motion	8
2.4.1.2 First law of thermodynamics	9
2.4.1.3 Moment of momentum	9
2.4.1.4 Euler work equation	10
2.4.2 Efficiency	11
2.4.2.1 Isentropic Efficiency	11
2.4.2.2 Polytropic Efficiency	12
2.4.2.3 Relationship between Polytropic and Isentropic efficiency	13
2.4.3 Real gas efficiencies	14
2.4.4 Surge	15
2.4.5 Choke	16
2.5 Gas Equations of State	17

3	Methods	21
3.1	Star-CCM+	21
3.1.1	Preparation of geometry in Star-CCM+	21
3.1.2	Meshing	23
3.1.3	Setting up of the fluid domain.	24
3.2	REFPROP	25
3.3	Grid independence study	26
3.4	Comparison between internal interface and mixing plane interface . .	28
4	Results	31
4.1	Isentropic efficiency study	31
4.2	The polytropic and isentropic efficiency	32
4.3	Turbulence model study	33
4.4	Gas models study	36
4.5	Effect of diffuser in the compressor	38
4.6	Analysis of flow characteristics inside the compressor	39
4.6.1	Design point analysis of compressor	40
4.6.2	Off-design operation analysis	42
4.6.2.1	Choke region	42
4.6.2.2	Surge region	45
4.7	Comparison of results between Star-CCM+ and ANSYS CFX	47
5	Conclusion	51
5.1	Future Work	51
	Bibliography	53
A	Appendix 1	I
B	Appendix 2	III
C	Appendix 3	V

List of Figures

2.1	A typical heat pump, taken from (Siemens Energy website) [1].	3
2.2	Air source heat pump diagram from (Lu, J et al.) [2].	4
2.3	Ground source heat pump schematic diagram from (Dincer, I et al.) [3].	5
2.4	Water source heat pump schematic diagram from (Ninikas, K. et al.) [4].	5
2.5	Heat Pump cycle, taken from (Siemens Energy website) [1].	6
2.6	Both views adapted from (Aungier, 2000) [5].	7
2.7	Control volume for a generalized turbomachine. Adapted from (Dixon, SL) [6].	9
2.8	Velocity triangles at impeller inlet and exit. Adapted from (Gravdahl & Egeland (2012)) [7]).	10
2.9	Reference reversible processes process for different efficiency definitions. Adapted from (Casey, M. 2021) [8].	11
2.10	h-s diagram of isentropic process (solid) and actual process (dashed) are shown. Taken from (Boles. and Cengel. 2015) [9].	12
2.11	h-s diagram of polytropic process (solid) and actual process (dashed) are shown. Taken from (Boles. and Cengel. 2015) [9].	13
2.12	Compressor map, adapted from [10].	15
2.13	Compressor characteristic curve, from [11].	16
2.14	P-h diagram of a gas. With region of focus on superheated gas region. Taken from (SWEF website) [12].	17
3.1	The fluid domain cut from the full compressor model.	22
3.2	The inlet, impeller and the diffuser domain of the final fluid volume respectively. The casing does not rotate in any of these regions. . . .	23
3.3	Meshing of the fluid domain. Casing not included in the picture. . . .	23
3.4	Meshing at the leading edge of the main blade.	24
3.5	Prism layer meshing at the boundary layer of the main blade.	24
3.6	Variation of c_p as a function of temperature.	26
3.7	Volume flow rate vs total pressure ratio plotted for different mesh cases.	27
3.8	Total pressure ratio vs isentropic efficiency plotted for different mesh cases.	28
3.9	Mixing plane interface between impeller and diffuser.	29
3.10	Internal interface plane interface between impeller and diffuser.	29

4.1	Difference between the isentropic efficiency generated by Star-CCM+ and Denton formula.	32
4.2	Difference between polytropic efficiency and isentropic efficiency plotted.	33
4.3	Volume flow rate vs total pressure ratio plotted for different turbulence model cases.	34
4.4	Total pressure ratio vs isentropic efficiency plotted for different turbulence model cases.	35
4.5	Volume flow rate vs total pressure ratio plotted for different real gas model cases.	36
4.6	Total pressure ratio vs isentropic efficiency plotted for different real gas model cases.	37
4.7	Comparison between isentropic efficiency of a compressor and of an impeller.	38
4.8	Compressor characteristic curve showing the operating point considered for analysis.	39
4.9	20%, 50% and 95% spanwise locations indicated as selected for analysis.	40
4.10	Analysis of relative Mach number at the inlet, impeller and diffuser at 20% spanwise location for design point operating condition.	41
4.11	Analysis of relative Mach number at the inlet, impeller and diffuser at 50% spanwise location for design point operating condition.	42
4.12	Analysis of relative Mach number at the inlet, impeller and diffuser at 95% spanwise location for design point operating condition.	42
4.13	Analysis of relative Mach number at the inlet, impeller and diffuser at 20% spanwise location for choking region operating condition.	44
4.14	Analysis of relative Mach number at the inlet, impeller and diffuser at 50% spanwise location for choking region operating condition.	44
4.15	Analysis of relative Mach number at the inlet, impeller and diffuser at 95% spanwise location for choking region operating condition.	45
4.16	Analysis of relative Mach number at the inlet, impeller and diffuser at 20% spanwise location for surge region operating condition.	46
4.17	Analysis of relative Mach number at the inlet, impeller and diffuser at 50% spanwise location for surge region operating condition.	46
4.18	Analysis of relative Mach number at the inlet, impeller and diffuser at 95% spanwise location for surge region operating condition.	47
4.19	Volume flow rate vs total pressure ratio plotted for Star-CCM+ and ANSYS CFX.	48
4.20	Total pressure ratio vs isentropic efficiency plotted for Star-CCM+ and ANSYS CFX.	48
A.1	Volume flow rate vs total pressure ratio plotted for the full range of simulation.	I
A.2	Total pressure ratio vs isentropic efficiency plotted for the full range of simulation.	II
B.1	Residuals - Choke region simulation.	IV
B.2	Residuals - Design point region simulation.	IV

B.3	Residuals - Surge region simulation.	IV
C.1	Analysis of Mach number at the impeller and diffuser at 20% spanwise location for choking region operating condition.	V
C.2	Analysis of Mach number at the impeller and diffuser at 50% spanwise location for choking region operating condition.	VI
C.3	Analysis of Mach number at the impeller and diffuser at 95% spanwise location for choking region operating condition.	VI
C.4	Analysis of Mach number at the impeller and diffuser at 20% spanwise location for design point operating condition.	VII
C.5	Analysis of Mach number at the impeller and diffuser at 50% spanwise location for design point operating condition.	VII
C.6	Analysis of Mach number at the impeller and diffuser at 95% spanwise location for design point operating condition.	VIII
C.7	Analysis of Mach number at the impeller and diffuser at 20% spanwise location for surge region operating condition.	VIII
C.8	Analysis of Mach number at the impeller and diffuser at 50% spanwise location for surge region operating condition.	IX
C.9	Analysis of Mach number at the impeller and diffuser at 95% spanwise location for surge region operating condition.	IX
C.10	Analysis of entropy at the impeller and diffuser at 20% spanwise location for choking region operating condition.	X
C.11	Analysis of entropy at the impeller and diffuser at 50% spanwise location for choking region operating condition.	X
C.12	Analysis of entropy at the impeller and diffuser at 95% spanwise location for choking region operating condition.	XI
C.13	Analysis of entropy at the impeller and diffuser at 20% spanwise location for design point operating condition.	XI
C.14	Analysis of entropy at the impeller and diffuser at 50% spanwise location for design point operating condition.	XII
C.15	Analysis of entropy at the impeller and diffuser at 95% spanwise location for design point operating condition.	XII
C.16	Analysis of entropy at the impeller and diffuser at 20% spanwise location for surge region operating condition.	XIII
C.17	Analysis of entropy at the impeller and diffuser at 50% spanwise location for surge region operating condition.	XIII
C.18	Analysis of entropy at the impeller and diffuser at 95% spanwise location for surge region operating condition.	XIV

List of Tables

3.1	Properties of R1234ze(E).	25
3.2	Number of mesh elements and their split-up.	26

1

Introduction

The greenhouse effect is the way in which heat is trapped close to Earth's surface by greenhouse gases (GHG) and high emissions of GHG are a threat to the stability of Earth's climate. But the global anthropogenic GHG emissions continue to rise even as the sea levels continue to rise. It appears that the largest contribution to the greenhouse effect stems from the emission of CO_2 . It is the number one contributor for the anthropogenic GHG, constituting about 75% which stem from the combustion of fossil fuel for transformation and use of energy [13].

GHG includes CO_2 , CH_4 , N_2O , and water vapor. Without the terrestrial greenhouse effect, the Earth's temperature would be about 33°C cooler. Since the beginning of the industrial era, human activities have increased the atmospheric CO_2 levels by about 50%. The atmospheric CO_2 level is about 417 ppm as of March 2022 [14].

The primary chemicals used as refrigerants include CFCs, HFCs and HCFCs which have been studied intensively because of their concerns about chlorine chemistry effects on stratospheric ozone. They are GHGs as they can absorb infrared radiation that can then exert additional radiative forcing that tends to warm the climate. The primary destruction of ozone in the stratosphere comes from the catalytic mechanisms involving various free radical species. Nitrogen oxides, chlorine oxides and hydrogen oxides participate in destruction of ozone. The chlorine catalytic mechanism is particularly efficient at destroying the ozone [15].

Global Warming Potential (GWP) is a measure of how much heat the emissions of GHG will absorb over time relative to the emissions of 1 ton of CO_2 . GWP of CO_2 is 1 as it is used as reference. The other GHGs have their GWP calculated based on the gas and the time frame. The larger the GWP, the more the GHG will heat up Earth compared to CO_2 . For example,

- Methane has a GWP of 25.
- Nitrous oxide has a GWP of 298.
- Common refrigerant Carbon tetrafluoride has a GWP of 7390.
- The refrigerant R134a has a GWP of 1430.
- The refrigerant R1234ze(E) has a GWP of 6.

District heating is a system of producing heat in a centralised location and transporting them to different locations through insulated pipes. It increases the overall system efficiency as the heat generation is coupled with electricity generation and waste incineration. It is possible to use biomass or geothermal as the fuel for heating

thereby reducing the CO_2 emissions. It is highly competitive when fuel prices are high [16].

The heat pump is one of the few ways for heat generation and it involves the use of refrigerants as the working fluid. With R134a being the common refrigerant for heat pumps in Scandinavia, it is estimated that if the heat pump loses 1% of its refrigerants every year, then it releases about 97.5 tons of CO_2 equivalents into the atmosphere [17].

1.1 Aim

- To develop the process of setting up and performing the simulation of a centrifugal compressor in Star-CCM+ using R1234ze(E) as the refrigerant.
- To evaluate the performance of the centrifugal compressor.

The focus is on the in-house design of a 2 stage centrifugal compressor for a heat pump which is used for district heating. The first stage of the centrifugal compressor is designed to handle a pressure ratio of 3 to 4. It is a centrifugal compressor with a vaneless diffuser and Inlet Guide Vanes (IGV) to regulate the airflow and pressure that enters the compressor. This type of compressor can handle high flow rate and high molecular weight (~ 100 g/mol) of the working fluid but unsuitable for high differential pressure. It was designed a few years ago and has been operated with an old refrigerant R134a which has a high GWP. It might therefore be a better solution environmentally if the working fluid can be replaced with R1234ze(E) which has a very low GWP.

1.2 Tools Used

- *Star-CCM+ 16.04.012-R8* - a commercial CFD code by Siemens.
- *REFPROP* - a computer program, distributed through the Standard Reference Data program of NIST, that provides thermophysical properties of pure fluids and mixtures over a wide range of fluid conditions including liquid, gas, and supercritical phases.

1.3 Limitations

1. Not focusing on the design aspect of the compressor.
2. Not focusing on creating speedline characteristics for multiple RPMs.
3. Focus is only on steady case assumption.

2

Theory

2.1 Heat pump

A heat pump is a system that is used to heat an enclosed space by transferring thermal energy from a cooler area to a warmer area. It operates based on the compression and expansion of a working fluid which is a refrigerant. The current generation of heat pumps are the improvements of the first developed systems by advancing on the scientific concepts and using more environmentally friendly refrigerants. The main components of a heat pump are: Expansion Valve, Evaporator, Compressor and a Condenser.

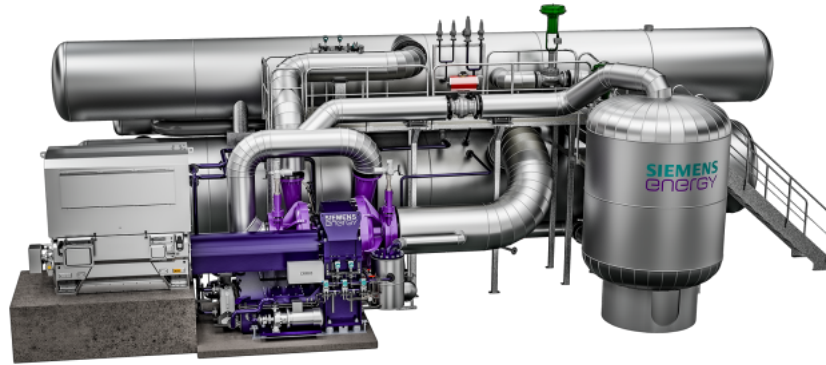


Figure 2.1: A typical heat pump, taken from (Siemens Energy website) [1].

The heat pumps can be classified into different categories based on different characteristics, like based on source of heat, based on operating cycle, based on the size of operation, based on the type of compressor used are a few of them.

2.1.1 Domestic heat pumps

First, domestic heat pumps are shown below and they are classified further based on source of high temperature, which are: air source heat pump, water source heat pump, ground source heat pump.

2.1.1.1 Air source heat pump

According to (Swedish Energy Agency) [18] this type of heat pump is used for domestic purposes and it draws heat from the outdoor air and transfers it to the water based heating system in the house. It can also be used for hot water in houses. They are easy and inexpensive to install and hence the most used one. The COP of this type of heat pump varies from 3 to 4 (Swedish Energy Agency) [18] depending on the weather outside.

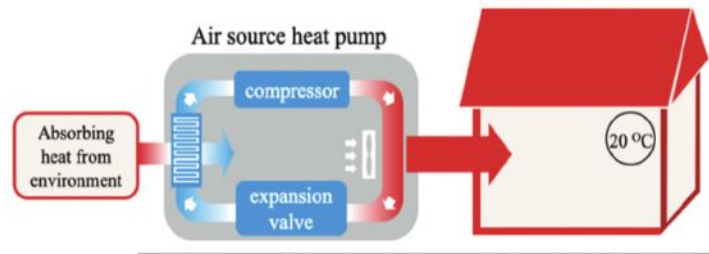


Figure 2.2: Air source heat pump diagram from (Lu, J et al.) [2].

2.1.1.2 Ground source heat pump

This type of heat pump functions with the heat source drawn from the soil or groundwater at about 9 m depth (Heat Pump.) [19]. This is used as a heat source as the temperature of the water remains relatively constant all year round. They are expensive to install because of the need to drill for placing the heat exchanger piping. The COP varies from about 3 to 4 (Heat Pump.) [19] depending on the where the heat is drawn.

From (Dincer, I et al.) [3], it is shown that they are also advantageous to use over air source heat pumps as the steady performance all year round results in it using fewer amount of refrigerants and also small annual energy consumption.

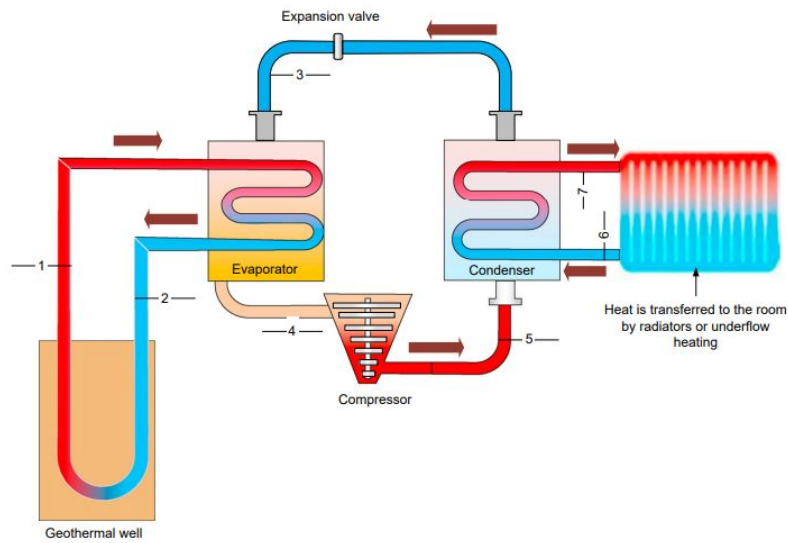


Figure 2.3: Ground source heat pump schematic diagram from (Dincer, I et al.) [3].

2.1.1.3 Water source heat pump

Water source heat pumps are similar to the ground source heat pump and the main difference being in the source from where the heat is drawn.

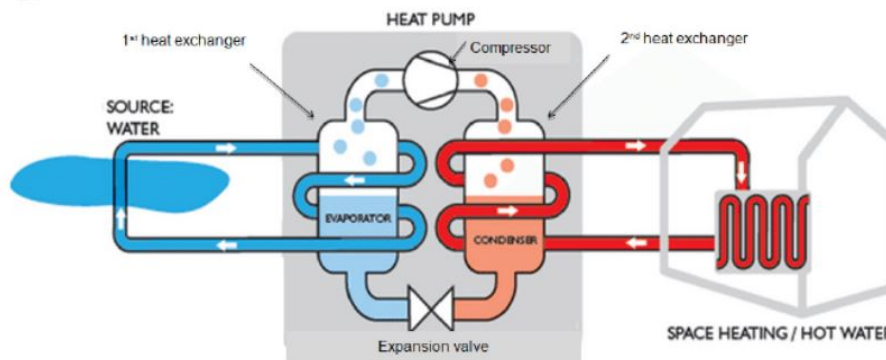


Figure 2.4: Water source heat pump schematic diagram from (Ninikas, K. et al.) [4].

For water source, wells or an open pond have been used commonly. When the ground and water sourced heat pumps are combined, they are termed geothermal heat pumps. The geothermal heat pumps are advantageous as they consume 33% less energy annually, and since they use groundwater or earth for source, they have a more stable source of energy than air as mentioned in (Lund, J.) [20].

2.1.2 Industrial scale heat pumps

Now, considering the industrial scale heat pumps, which are generally much larger physically (Figure 2.1) than the domestic ones and also produce much more heat when compared to the domestic ones. In this type of heat pump, the heat can even be taken from low temperature heat source and can be used to heat up the refrigerant flowing in the pipes which in turn gets compressed to become even hot, which is then sent to supply heat for district heating (or to Condenser) which is a common example of such large scale heat pumps. The refrigerant then becomes warm from losing heat and is then sent past an expansion valve where it expands and becomes a cold liquid. Then it is again sent into the Evaporator and the process begins once again. The heat pump used in Figure 2.1, has a turbomachinery centrifugal compressor for compressing the working fluid. There are also other types of compressors like screw type ones which are used for certain specific applications.

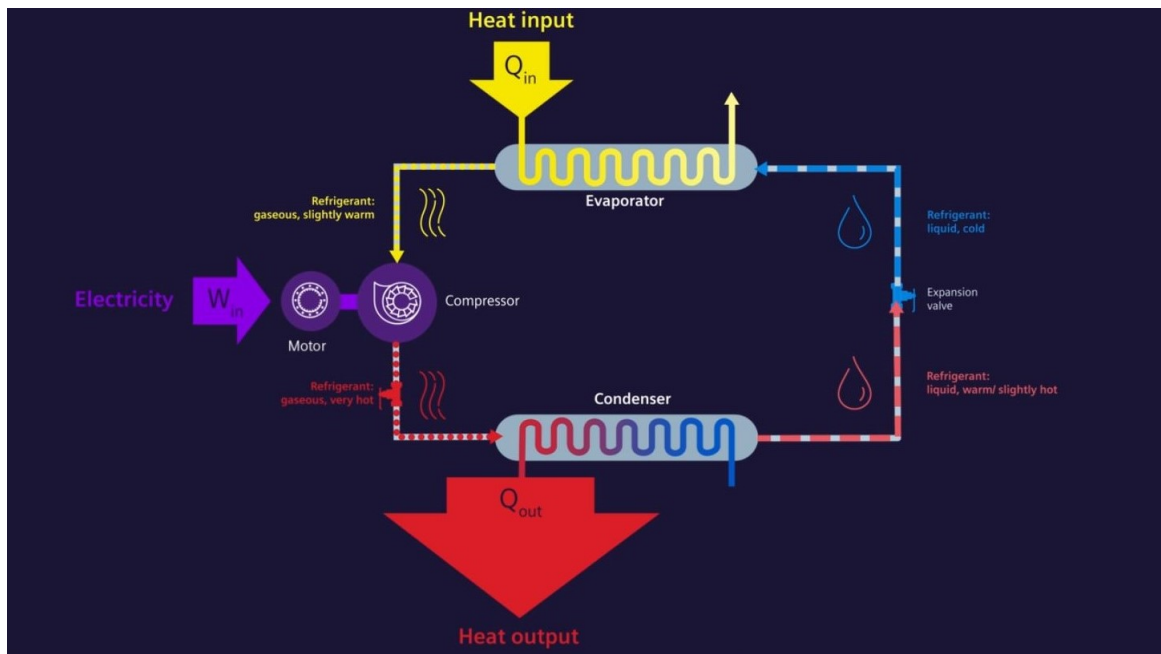


Figure 2.5: Heat Pump cycle, taken from (Siemens Energy website) [1].

2.2 Centrifugal compressor

The compressors can be classified into two categories namely, positive displacement and dynamic and the centrifugal compressor comes under the category of dynamic compressor. It is a turbomachine which employs centrifugal effects to increase the fluid pressure. For the application of aircraft propulsion, the axial flow compressors were better as it was able to meet the need of large engines. It has smaller frontal area and hence reduced drag for a given engine and also had a higher efficiency of about 3% or 4% when compared to centrifugal compressor. But for very small compressors with low flow rates, the axial compressor efficiency dropped sharply (Dixon, SL.) [6]. An image of centrifugal compressor with its components labelled

is shown in Figure 2.6.

For applications like refrigeration plants and compression-type heat pumps used for district heating, the centrifugal compressor is commonly used for their good economy, low maintenance and reliability.

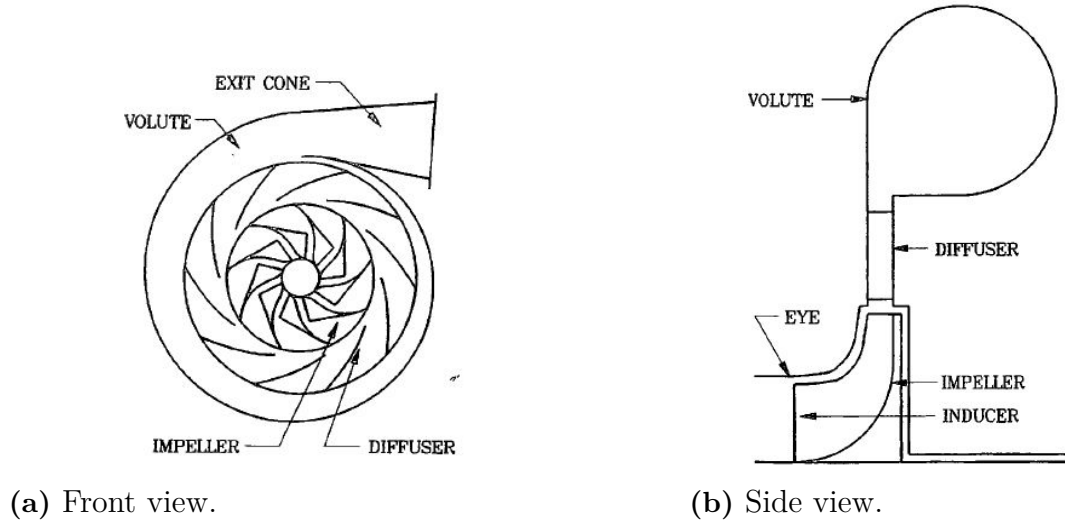


Figure 2.6: Both views adapted from (Aungier, 2000) [5].

2.3 Components of a centrifugal compressor

The main components of a centrifugal compressor are: Inlet Guide Vanes (IGVs), impeller, shroud, diffuser and volute.

IGVs are usually located upstream of the compressor where they can influence and regulate the airflow and pressure entering the first stage of the compressor. There are both fixed and adjustable guide vanes which can be used to guide the fluid flow efficiently into the compressor. Adjustable IGVs can help the fluid to enter the first stage of the compressor with a pre-swirl. The pre-swirled fluid entering the impeller needs less work from the blades to be turned by it in the required direction. The angle of the pre-swirled flow increases as the IGV closes thereby reducing the stress on the impeller as the incoming flow angle matches the direction of rotation. The inlet guide vanes can be used to increase or reduce the work done by the compressor.

Impellers are selected based on their aerodynamic performance and mechanical integrity. The impellers are of two types namely semi-open and closed. In semi-open, the blades are attached to the hub and rotate together with no cover/shroud, while in closed, the hub and blades are attached and there is also a cover/shroud which is also attached to the blades. To distinguish between the impellers, the term flow coefficient (ϕ_1) is used. Where, $\phi_1 = \frac{Q_1}{(D_2)^3 N}$ and Q_1 is the inlet flow, D_2 is the tip diameter and N is the rotational speed [21]. The higher the flow coefficient value, the higher the volume flowing through the compressor.

The shroud is a cover attached to the blade at the outer wall which rotates with the impeller. These types of impellers are generally called shrouded impellers and they are commonly used in multistage industrial compressors (Aungier, 2000) [5].

Diffusers are used to convert the kinetic energy of the fluid exiting the impeller into static pressure rise. The way it can be achieved is by increasing the flow area thereby reducing flow velocity and increasing the static pressure. Another way to do that is to change the flow mean path radius which reduces the tangential velocity and increases static pressure (Turunen-Saaresti T) [22]. This is generally performed using a vaneless or a vaned diffuser. Where the latter achieves better pressure rise and higher efficiency than the former (Turunen-Saaresti T) [22]. The vaneless diffuser is mainly used for large operation range and most commonly used in operations involving process, refrigeration and turbochargers.

A volute in a centrifugal compressor collects the flow from blade cascades and deliver it to the exit. The volute also converts the flow kinetic energy to static pressure rise. The flow in this region is complicated as it involves separated, reversed and vortical flow zones.

2.4 Compressor Performance

The compressor characteristics like pressure ratio, mass flow rate and efficiency can be used to evaluate the performance of a compressor and to establish the operating range of it.

2.4.1 Work

2.4.1.1 Newton's second law of motion

Starting from the first principle of Newton's second law of motion, which states that the rate of change of momentum of a system with respect to time is related to the force applied to the system. If the net force on the system is not zero, then the imbalance in force, makes the system accelerate in the direction of force.

$$\sum \vec{F}_x = \frac{d}{dt} (m\vec{V}_x) = m\vec{a}_x \quad (2.1)$$

For a system like compressor which only has a single inlet and outlet (single stream process), the above equation can be remodeled as,

$$\sum \vec{F}_x = \dot{m}_o \vec{V}_o - \dot{m}_i \vec{V}_i \quad (2.2)$$

where the \vec{V}_o is the steady flow velocity exiting the control volume and the \vec{V}_i is the steady flow velocity entering the control volume.

2.4.1.2 First law of thermodynamics

The compressor is a control volume where the first law of thermodynamics is followed, where the first law states that the energy can neither be created nor destroyed, it can only change form, which is also called *conservation of energy principle*.

$$E_{in} - E_{out} = \Delta E_{system}$$

Similarly, according to the *conservation of mass principle*, the net mass transfer entering or leaving a control volume during a time interval Δt is equal to the net change of total mass within the control volume during Δt .

$$m_{in} - m_{out} = \Delta m_{CV}$$

2.4.1.3 Moment of momentum

Applying the principles of Newton's second law of motion to centrifugal compressors is of central importance to analyse the energy transfer.

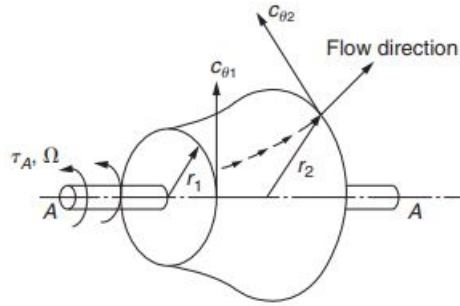


Figure 2.7: Control volume for a generalized turbomachine. Adapted from (Dixon, SL) [6].

For a system with mass m the time rate of change of angular momentum is equal to the vector sum of moments of all external forces acting on the system for some arbitrary axis A-A.

$$\tau_A = m \frac{d}{dt} (r C_\theta) \quad (2.3)$$

This is the angular momentum equation where the r is the distance from the mass center of the axis of rotation. C_θ is the tangential velocity which is perpendicular to both radius and the axis. By applying a control volume around the impeller of the compressor as shown in Figure 2.7, where the swirling fluid enters the volume at radius r_1 with a tangential velocity $C_{\theta 1}$ and exits r_2 with a tangential velocity of $C_{\theta 2}$. The angular momentum equation for one dimensional steady flow becomes,

$$\tau_A = \dot{m} (r_2 C_{\theta 2} - r_1 C_{\theta 1}) \quad (2.4)$$

2.4.1.4 Euler work equation

For a compressor rotor rotating at angular velocity of ω , the rate of work done on the fluid is given by

$$\dot{W}_c = \tau_A \omega = \dot{m} (U_2 C_{\theta 2} - U_1 C_{\theta 1}) \quad (2.5)$$

where $U = \omega r$. The relationship between torque and specific work is

$$\Delta W_c = \frac{\dot{W}_c}{\dot{m}} = \frac{\tau_A \omega}{\dot{m}} = (U_2 C_{\theta 2} - U_1 C_{\theta 1}) > 0 \quad (2.6)$$

This is known as the *Euler equation*.

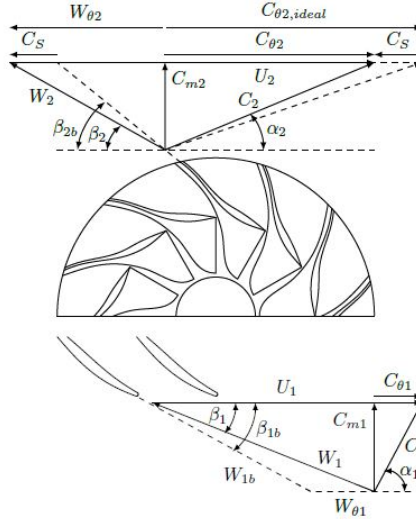


Figure 2.8: Velocity triangles at impeller inlet and exit. Adapted from (Gravdahl & Egeland (2012)) [7]).

The compressor sometimes is fitted with an IGV and the main role of it being to give absolute tangential velocity component to the flow at the inlet, ($C_{\theta 1} \neq 0$). But depending on the direction in which the IGV whirls the flow can affect the work done by the compressor. For instance, if the pre-whirl is $C_{\theta 1} > 0$, then the flow is already turned in the direction in which the impeller is rotating and hence the impeller has to do less work to turn it. But if the $C_{\theta 1} < 0$ then the impeller has to perform extra work to overcome the opposing flow. The flow has $C_{\theta 1} = 0$ without the IGV and hence the effect of IGV on the Euler pump equation is quite clear, as without it, the eq. 2.6 becomes,

$$\Delta W_c = U_2 C_{\theta 2}$$

2.4.2 Efficiency

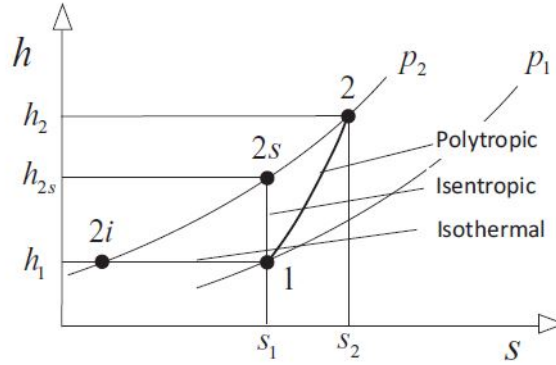


Figure 2.9: Reference reversible processes process for different efficiency definitions. Adapted from (Casey, M. 2021) [8].

The selection of reversible process to be used as ideal reference depends on the convention and application of the machine (Casey, M. 2021) [8].

The isentropic efficiency is the easiest to understand and it considers the relevant reversible process to be an isentropic process to be from the states 1 to 2s between the inlet and outlet pressure levels. There is no heat transfer involved hence it is also called as adiabatic efficiency.

The polytropic on the other hand considers it to be a reversible process whose static state coincides with the actual change of state of gas in the compressor from state 1 to 2. Not adiabatic as heat is added to bring a change of state along the reversible path.

In the isothermal efficiency, the reference process considered is a reversible process between the inlet and outlet pressure levels having the same temperature of gas at inlet from state 1 to 2i. Since ideal isothermic process is not adiabatic, this efficiency is not adiabatic.

2.4.2.1 Isentropic Efficiency

For a machine which absorbs work, the efficiency is given as a ratio between the ideal change in energy and actual change in energy. And in the case of isentropic efficiency, the ideal process is the isentropic process in which the energy change is the lowest.

The isentropic efficiency of a compressor is defined as the isentropic enthalpy rise over an impeller divided by the actual enthalpy rise over the impeller.

$$\eta_{tt} = \frac{\text{isentropic enthalpy rise}}{\text{actual enthalpy rise}} = \frac{h_{02}^{is} - h_{01}}{h_{02} - h_{01}} \quad (2.7)$$

Where, the superscript *is* denotes that the quantity is estimated via the isentropic relations and the subscript *0* refers to the total values. The above equation eq. 2.7 can then be rewritten as

$$\eta_{tt} = \frac{T_{02}^{is} - T_{01}}{T_{02} - T_{01}} \quad (2.8)$$

where eqn. 2.8 with the help of the relation $h=h(t)$, which then with the help of specific heat expression, becomes,

$$h = c_p(T)dT$$

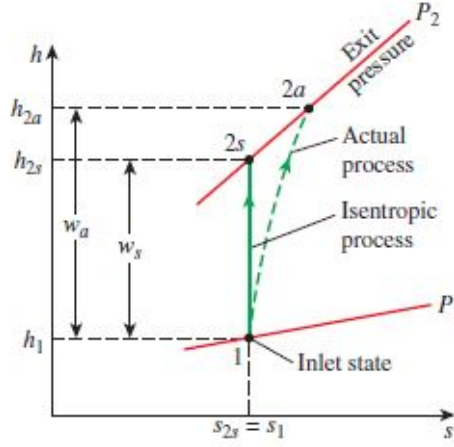


Figure 2.10: h-s diagram of isentropic process (solid) and actual process (dashed) are shown. Taken from (Boles. and Cengel. 2015) [9].

The compressor is usually driven by a turbine which extracts energy from hot exhaust gases. Transonic flow conditions are reached in parts of the compressor map, a realistic relation is used to assess the actual temperatures. The ideal temperature rise results due to the gas compression from the P_{01} the inlet total pressure to P_{02} the outlet total pressure. Hence using the isentropic relations,

$$\frac{T_{02}^{is}}{T_{01}} = \left(\frac{P_{02}}{P_{01}} \right)^{\frac{\gamma-1}{\gamma}} \quad (2.9)$$

hence, $T_{02}^{is} = T_{01} \left(\frac{P_{02}}{P_{01}} \right)^{\frac{\gamma-1}{\gamma}}$ which leads the isentropic efficiency to be,

$$\eta_{tt} = \frac{T_{01}}{T_{02} - T_{01}} \left(\left(\frac{p_{02}}{p_{01}} \right)^{\frac{\gamma-1}{\gamma}} - 1 \right) \quad (2.10)$$

2.4.2.2 Polytropic Efficiency

The difference between the Polytropic and the Isentropic efficiency is given before and it is that the reference process is a reversible compression path from state 1 to 2.

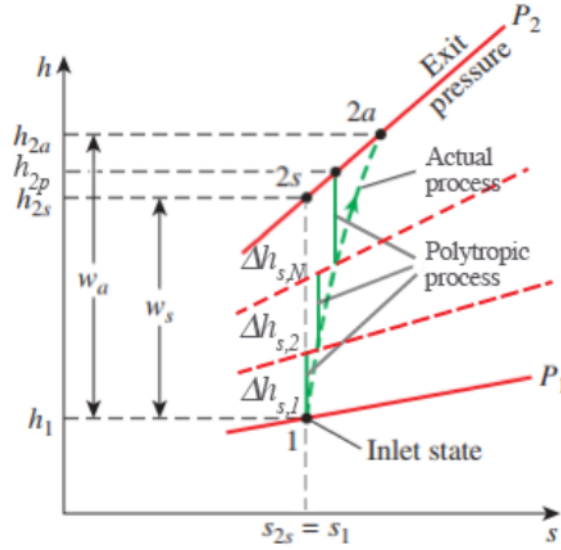


Figure 2.11: h-s diagram of polytropic process (solid) and actual process (dashed) are shown. Taken from (Boles. and Cengel. 2015) [9].

Looking at the above figure, the small-scale polytropic efficiency is defined as the ratio between the reversible enthalpy change to the real enthalpy change,

$$\eta_p = \frac{v dp}{dh} = \frac{dh - T ds}{dh} = \frac{1 - T ds}{dh} \quad (2.11)$$

To calculate the aerodynamic work done along this path, the integration of the aerodynamic work has to be carried out.

$$\eta_p = \frac{\int_1^2 v dp}{\int_1^2 dh} = \frac{\int_1^2 v dp}{h_2 - h_1} = \frac{y_{12}}{h_2 - h_1} \quad (2.12)$$

This requires the detailed knowledge of the thermodynamic properties along the actual path which is not available in practice.

The total-total polytropic efficiency is then given by

$$\eta_p^{tt} = \frac{y_{12} + 1/2(c_2^2 - c_1^2)}{w_{s12}} = \frac{\int_1^2 v dp + 1/2(c_2^2 - c_1^2)}{w_{s12}} \quad (2.13)$$

And after performing some substitutions, it finally becomes,

$$\eta_p^{tt} = \frac{\gamma - 1}{\gamma} \frac{\ln(P_{02}/P_{01})}{\ln(T_{02}/T_{01})} \quad (2.14)$$

This is not the true polytropic efficiency as this is based on reversible work of total conditions from 1 to 2 rather than considering the static work and the kinetic energy separately.

2.4.2.3 Relationship between Polytropic and Isentropic efficiency

For a compression process, the polytropic coefficient γ is related to the isentropic coefficient κ through

$$\frac{\gamma - 1}{\gamma} = \frac{1}{\eta_p} \frac{\kappa - 1}{\kappa} \quad (2.15)$$

The polytropic relationship between the stagnation pressure ratio and temperature ratio for an ideal gas in a compression process is given by

$$\left(\frac{p_{02}}{p_{01}}\right)^{\left(\frac{\kappa-1}{\kappa}\right)} = \left(\frac{T_{02}}{T_{01}}\right) \quad (2.16)$$

By combining the equations 2.9, 2.15 and 2.16 into the equation 2.8, we get the isentropic and the polytropic efficiency which are dependent on each other as (Karlsson, A., 2018) [23],

$$\eta_{tt} = \left[\left(\frac{P_{02}}{P_{01}}\right)^{\left(\frac{\kappa-1}{\kappa}\right)} - 1 \right] / \left[\left(\frac{P_{02}}{P_{01}}\right)^{\left(\frac{1}{\eta_p} \frac{\kappa-1}{\kappa}\right)} - 1 \right] \quad (2.17)$$

$$\eta_p = \frac{\left(\frac{\kappa-1}{\kappa}\right) \log\left(\frac{P_{02}}{P_{01}}\right)}{\log \left[\left(\left(\frac{P_{02}}{P_{01}}\right)^{\frac{\kappa-1}{\kappa}} - 1\right) \frac{1}{\eta_{tt}} + 1 \right]} \quad (2.18)$$

2.4.3 Real gas efficiencies

The above equations of efficiencies are perfectly suitable for ideal gases or calorically perfect gases where the gas properties such as C_p , C_v and γ are constant throughout the process. Since in this work, the gases are not ideal and do not have constant C_p , C_v and γ , the equations 2.8, 2.17 and 2.18 are not suitable as the simplification of the formulas lead to inaccurate results.

The progression from the equation 2.7 to 2.8 can only be done if the C_p is assumed to be constant which is not the case here. Hence for computing the Isentropic efficiency, the equation 2.7 can be used but which leads to the term h_{02}^{is} whose real value cannot be determined by hand. The determination of h_{02}^{is} requires the C_p at the outlet boundary and the T_{02}^{is} the outlet boundary isentropic temperature. It is possible to determine the C_p as it given as function of temperature when defining the fluid property in the Star-CCM+ but the T_{02}^{is} cannot be determined without equation 2.9 which has a constant value of γ . This approximation of γ yields incorrect values of T_{02}^{is} and hence incorrect isentropic efficiency.

Star-CCM+ has the option of generating isentropic efficiency report for a given system and it had been utilized to determine the efficiency of the system. Star-CCM+ utilises equation 2.7 directly to determine the efficiency and generating the value in the end. The way it does it is by computing the total enthalpy for the inlet and outlet boundaries and also the isentropic total enthalpy and substituting them in the equation 2.7. According to the (Star-CCM+ support) [24], the determination of the total enthalpy is done by using the formula,

$$h_o = h + \frac{1}{2}c^2$$

This leads to the efficiency value which is close to the real value.

For isentropic efficiency, another form of the equation is obtained from (*Denton J., 1993*) [25] which is written as,

$$\eta_{tt} = 1 - \frac{T_{02}(s_2 - s_1)}{(h_{02} - h_{01})} \quad (2.19)$$

This equation involves the calculation of isentropic efficiency from other variables and does not require a constant γ and hence there is no approximation and the values obtained from this equation closely matches the value obtained from equation 2.7. The Polytropic efficiency equation is obtained from ANSYS CFX which is written as

$$\eta_p = 1 - \frac{(T_{02} - T_{01})(s_2 - s_1)}{(\ln(\frac{T_{02}}{T_{01}}))(h_{02} - h_{01})} \quad (2.20)$$

Which is not dependent on averaged γ and hence the result from this equation is acceptable.

2.4.4 Surge

Surge is a global flow instability occurring in the centrifugal compressor at a specific speed line at low mass flow rate operation. It describes the violent air flow oscillating in the axial direction of the compressor which indicates that the axial velocity is fluctuating and may also attain negative values. It is generally classified into deep surge and mild surge where the one with the negative mass flow rate is generally termed a deep surge and the one without the reversed flow is termed a mild surge [10]. It is given in a sample compressor map as shown below in Figure 2.12.

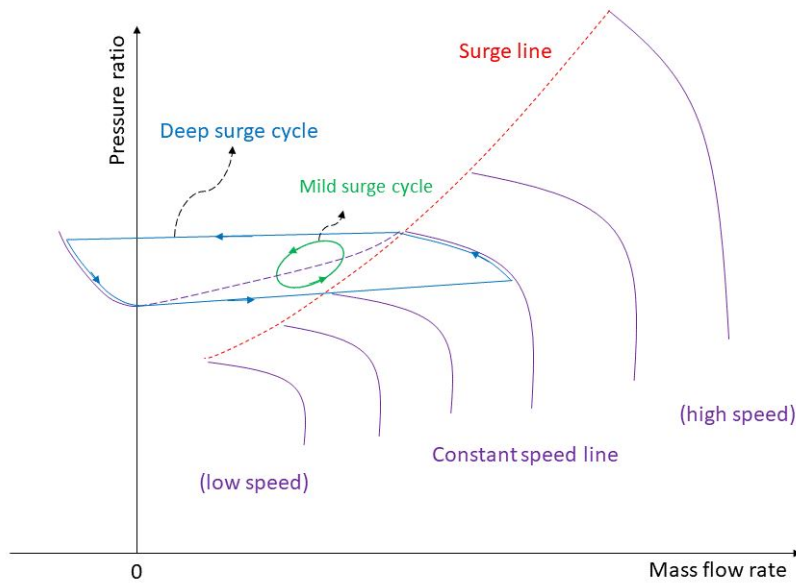


Figure 2.12: Compressor map, adapted from [10].

The surge is generally observed when the mass flow rate through the compressor reduces as the outlet pressure increases for a given operating speed/constant rotational speed, which can be observed in the above figure. The internal flow faces an adverse pressure gradient and gets destabilized and results in flow reversal (Semlitsch B., et al.) [26]. It affects the blades by causing large vibratory stress in the blades thereby leading to the breakdown of operability of the compressor. There are many active and passive methods for controlling the flows and to increase the operation range of the centrifugal compressor and the use of a ported shroud is one of them which can be used to increase the surge margins by allowing some flow to recirculate from the blade passage back into the compressor inlet (Semlitsch B., et al.) [26]. Also another passive flow control method called self-regulating-casing-treatment (SRCT) as shown by (Yang, M., et al.) [27] which helps in enhancing stability by removing the secondary flow which originates from the main blade tip from the passage by the downstream slot of SRCT when the compressor approaches surge.

2.4.5 Choke

Choking is a phenomenon that occurs at high mass flow rates through the compressor and the flow through the compressor cannot be increased further as the Mach number reaches unity at some parts of the compressor and hence the flow is said to be choked.

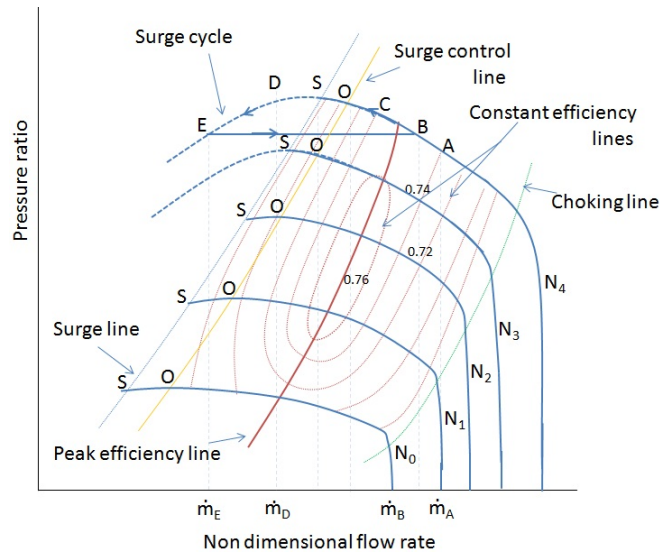


Figure 2.13: Compressor characteristic curve, from [11].

It is observed in the above figure, that the mass flow rate of the characteristic curve does not increase after the *Choking line* and it stays constant. This behavior is termed choking as the mass flow rate through the compressor cannot be any higher than this and is almost constant for low pressure ratios. This effect is mainly observed in the low outlet pressure case. Choking occurs due to two main reasons, they are,

1. If the inlet flow is subsonic and the flow will choke if the Mach number reaches unity at the throat between the blades.

2. If the inlet is supersonic, the flow will remain supersonic up until the throat of the blade until it reaches a normal or an oblique shock at the throat. The flow is choked until this point and if the back pressure is reduced under these conditions, the shock in the passageway moves further downstream but there is no change in the upstream flow properties.

2.5 Gas Equations of State

Centrifugal compressors are generally applied to wide range of problems and tasks where it encounters a wide variety of gases and gas mixtures span over a broad range of pressure and temperature. In many of these cases, the gas may not behave in an ideal manner and hence requires models to mimic the non-ideal behavior which are called real gas models. Furthermore, the fluid might be gas, liquid or both. Since the centrifugal compressor is rarely used for two phase flow, modelling of the gas phase covers the region of interest. The P-h diagram for a fluid is given below.

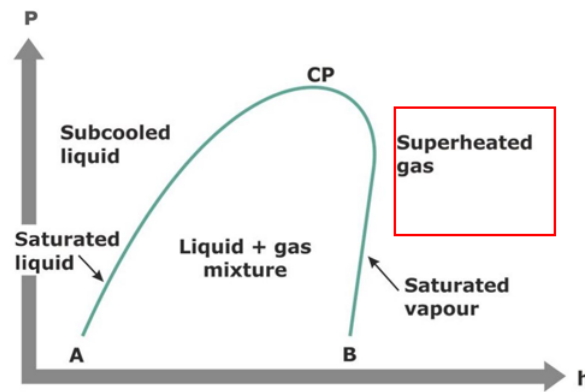


Figure 2.14: P-h diagram of a gas. With region of focus on superheated gas region. Taken from (SWEP website) [12].

In this work, the refrigerant is in the superheated region and the simulations are performed with conditions just after the saturated vapour region. It is desirable to avoid venturing into the saturation region to ensure that the compressor does not face two phase flows.

There are various real gas models available in literature and some of them are discussed below. All the models start with the basic equation,

$$pv = RT \quad (2.21)$$

Where p = pressure

v = specific volume

R = universal gas constant

T = absolute temperature

Van der Waals

Van der Waals modified the basic equation 2.21 with v-b to account for the volume that the gas particles occupy, and also changed pressure to $(p+a/v^2)$ (Tsonopoulos, C., et al.) [28]. The equation finally becomes,

$$(p + a/v^2)(v - b) = RT \quad (2.22)$$

Where **a** is the measure of attractive forces and **b** is the co-volume of the particles and their values are evaluated based on experimental observation and which leads to the following values,

$$a = \frac{27R^2T_c^2}{64P_c}, \quad b = \frac{1}{8} \frac{RT_c}{P_c}$$

With T_c and P_c being critical temperature and critical pressure.

Redlich-Kwong

The Redlich-Kwong model equation is,

$$p = \frac{RT}{(v - b)} - \frac{a}{[T^{0.5}v(v + b)]} \quad (2.23)$$

where

$$a = \frac{0.4275R^2T_c^2}{P_c}, \quad b = \frac{0.0867RT_c}{P_c}$$

The simple 2 parameter real gas equation of state is adequate for most of the centrifugal compressor analyses and also offer very good computational speed. It is one of the most accurate 2 parameter equations except for the points close to the critical point [5].

Soave-Redlich-Kwong

Soave modified the Redlich-Kwong model where he replaced the $T^{0.5}$ in the equation 2.23 with an equation which was dependent on temperature. This change improved the prediction for liquid densities and vapor liquid equilibrium [29]. The equation is,

$$p = \frac{RT}{v - b} - \frac{a\alpha(T_r)}{v(v + b)} \quad (2.24)$$

where, $\alpha(T_r) = [1 + (0.48 + 1.574\omega - 0.176\omega^2)(1 - T_r^{0.5})]^2$ and

$$a = \frac{0.42748R^2T_c^2}{P_c}, \quad b = \frac{0.08664RT_c}{P_c}$$

ω = accentric factor.

α = attractive term in the original Redlich-Kwong equation.

Modified Soave-Redlich-Kwong

Graboski and Daubert modified the Soave-Redlich-Kwong model to improve its behavior for phase equilibrium calculations that involve non-polar molecules (Graboski

& Daubert) [30] and [31]. All the equations are identical to Soave-Redlich-Kwong model except the $\alpha(T_r)$ equation. Where,

$$\alpha(T_r) = \left[1 + \left(0.48503 + 1.55171\omega - 0.15613\omega^2 \right) \left(1 - T_r^{0.5} \right) \right]^2 \quad (2.25)$$

ω = accentric factor.

P_r = Reduced pressure.

T_r = Reduced temperature.

Peng-Robinson

Peng-Robinson equation also focuses typically towards the vapor liquid like the Soave-Redlich-Kwong model, but giving better results in the estimation of liquid phase density. Peng and Robinson modified the Redlich-Kwong equation, as

$$p = \frac{RT}{V_m - b} - \frac{a\alpha}{V_m(V_m + b) + b(V_m - b)} \quad (2.26)$$

The a , b and α being modified as well,

$$\begin{aligned} a &= \frac{0.457235R^2T_c^2}{p_c} \\ b &= \frac{0.077796RT_c}{p_c} \\ \alpha &= \left(1 + \left(0.37464 + 1.54226\omega - 0.26992\omega^2 \right) \left(1 - \sqrt{T_r} \right) \right)^2 \end{aligned}$$

With T_c and P_c being critical temperature and critical pressure.

α = attractive term in the original Redlich-Kwong equation.

3

Methods

To achieve the results two pieces of softwares were used to prepare the geometry and the working fluid. One for performing the CFD simulation and the other is for obtaining the thermodynamic and fluid properties of the refrigerant. Steps performed in both the softwares are discussed here.

3.1 Star-CCM+

All the major work involving the geometry, simulation and the post processing were performed in *Siemens Star CCM + 2021.2.1 16.04.012-R8* where the R8 indicates the double precision.

3.1.1 Preparation of geometry in Star-CCM+

The compressor in focus is a centrifugal compressor with ten main blades and ten splitter blades and all are backswept. The diffuser is a vaneless diffuser. The inlet part is a cylinder extended from the eye of the impeller to make sure that the flow enters the impeller uniformly.

The simulations are performed for one blade row and not for the entire compressor as the flow inside the fluid domain between two blades is identical for the whole compressor.

The compressor model was prepared and provided as a .vda file. This file contains the information about the blades, hub and casing in the form of three dimensional coordinates. More specifically, for the main blade and splitter blade, it contains the outline of the blade spanning from LE to TE and from hub to tip, thereby blade surface can be filled manually. For hub and casing of the compressor, there is just a line spanning from the inlet to the outlet. There was no details about the inlet or diffuser part in this file and hence the coordinate files had to be created manually.

Star-CCM+ accepts the .vda file format for importing a CAD geometry and hence it was used to generate the main blade and splitter blade's pressure and suction surfaces. The hub and tip surfaces of the blades had to be filled manually and all the surfaces had to be sewn together to create a solid body from the sheet bodies. For the hub and casing, the coordinates were extracted from the .vda file and stored in a .csv file. The .vda file model had no tip gap between the blades and the casing

and hence when creating the casing .csv file, a tip gap of 0.7 mm was added. Then both the files were imported as Spline under the import 3D curve option so that CAD operations like revolving, bridging and others could be performed. The lines were then revolved with z-axis as the axis of rotation to generate the hub and casing surface.

After preparing the basic compressor housing geometry, the inlet to the compressor was extended by about 120 mm to make sure that the flow to the compressor is uniform. It was done the same way the hub and casing were generated. By importing the line and then revolving it. The diffuser is then added to the inlet-housing geometry whose sketch and dimensions were provided and the coordinates were created accordingly. Then the whole geometry was united and then boolean subtraction was performed between the full housing and the blades. This led to the body being ready to be used for the Turbo Slicing option which is an in-built tool in Star-CCM+ to help generate the neutral surface which can be used to slice the full geometry to get the fluid volume required for the simulations. But since it did not work for this geometry, the neutral surface had to be created manually which followed the blade geometry by using the blade coordinates to make sure they are following a proper path as seen below in Figure. 3.1.

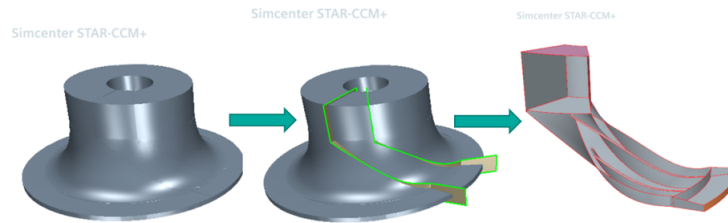


Figure 3.1: The fluid domain cut from the full compressor model.

The neutral surface seen in Figure. 3.1 is actually a single sheet body which is then copied and pasted at an angle of 36° to make sure that the blades are in between the neutral surfaces. Then the compressor housing is sliced by these two surfaces and the fluid domain is obtained. Then finally the fluid domain is sliced into 3 different sections to give rotation only to the specific part. The three parts can be widely classified into inlet domain, impeller domain and diffuser domain as shown in Figure. 3.2. It can also be seen if the region is rotating or not. But it is to be noted that the casing does not rotate in any of the region.

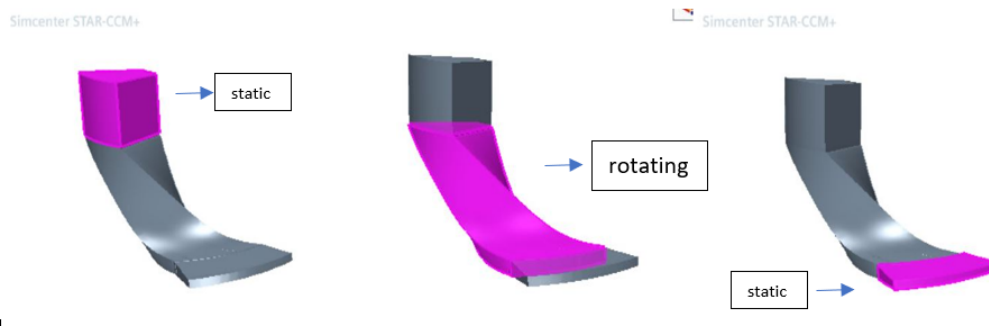


Figure 3.2: The inlet, impeller and the diffuser domain of the final fluid volume respectively. The casing does not rotate in any of these regions.

3.1.2 Meshing

Once the bodies are sliced into three different regions, the geometry is ready to be meshed. For meshing, a Polyhedral Mesher was used with five prism layers at the compressor walls with 1.5 stretching. But custom controls were applied to the blades surface by first meshing it with a quad dominant mesher on the surface, then changing the base number of prism layers to ten with 1.5 stretching at the surface. Wake refinement was also performed with finer mesh following the trailing edge of the blades into the diffuser. The total meshing activity amounts to approximately 5.85M mesh elements for the final model in the total fluid volume with 2.37×10^5 cells in the inlet, 4.98M cells in the impeller region and 2.650×10^5 cells in the diffuser. The below figures show the meshing of the total fluid volume, the meshing at the leading edge of the main blade and the prism layer meshing at the boundary of main blade.

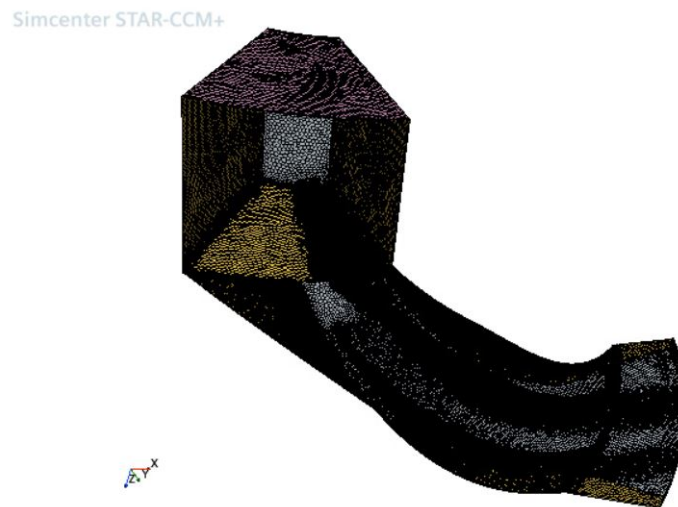


Figure 3.3: Meshing of the fluid domain. Casing not included in the picture.

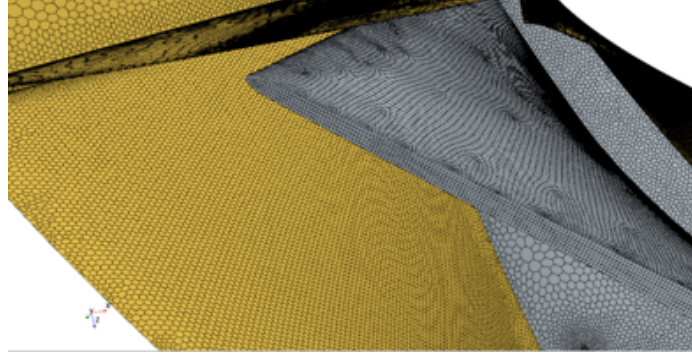


Figure 3.4: Meshing at the leading edge of the main blade.

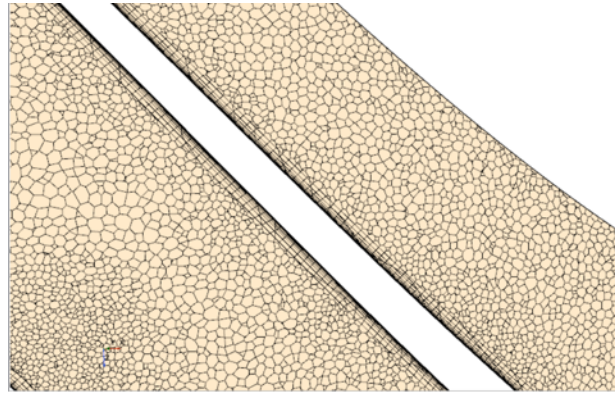


Figure 3.5: Prism layer meshing at the boundary layer of the main blade.

3.1.3 Setting up of the fluid domain.

The inlet is defined as a stagnation inlet with total pressure and total temperature as the boundary conditions. The outlet boundary is defined as a pressure outlet where the pressure is specified according to the operating point.

A rotating reference frame is created with the z-axis as the axis of rotation and the RPM of 7635 is given. It is then assigned to the Impeller region with all the boundaries being given the Region Reference frame specification except the casing boundary whose reference frame is specified as Lab Reference Frame. A periodic boundary condition is given to the side walls of the fluid domain. The interface essentially connects the side boundaries which are physically separated by an angle of 36° by mapping them to each other and the information is translated across the boundaries. An interface is created between the Inlet region exit and the Impeller region entry and a similar interface is created at the Impeller exit and the Diffuser entry. Both the interfaces are modelled as an Internal interface instead of Mixing plane type interface, as at the interface, circumferentially averaged flow field data is transferred in a conservative manner between two rotationally periodic regions in case of mixing plane interface which is not preferred. More about that can be seen in chapter 3.4.

The simulations are performed in a steady state condition. Second order implicit Coupled solver is used for the flow with coupled energy. Together they solve the conservation equations for mass, momentum, and energy simultaneously using a time- (or pseudo-time-) marching approach.. It is an alternative to the density-based and pressure-based segregated algorithm with SIMPLE-type pressure-velocity coupling. The $k-\omega$ SST model is used as the turbulence model. The working fluid is a refrigerant R1234ze(E) and Real gas law with Redlich Kwong gas model was used. The reference pressure is set to zero bar. Studies to see the difference between the turbulence model, gas model and number of mesh elements are discussed in the later sections.

3.2 REFPROP

According to NIST, REFPROP is a computer program, distributed through the Standard Reference Data program of NIST, that provides thermophysical properties of pure fluids and mixtures over a wide range of fluid conditions including liquid, gas, and supercritical phases.

The working fluid properties are set up by entering the values of the properties selected based on the requirements which are obtained from (REFPROP) [32].

Properties	Equations
Accentric factor	0.313
Critical Pressure	3634936.85 Pa
Critical Temperature	382.52 K
Molecular weight	114.0 kg/kmol

Table 3.1: Properties of R1234ze(E).

The following properties are also defined for the fluid, but provided as a function of temperature rather than constants.

The dynamic viscosity equation (μ) [Pa · s]

$$- 5.19468E^{-5}T^0 + 5.43837E^{-7}T^1 - 1.68201E^{-9}T^2 + 1.94476E^{-12}T^3 \quad (3.1)$$

The specific heat equation (c_p) [kJ/kg · K]

$$11749.1308T^0 - 164.156462T^1 + 0.908871794T^2 - 0.00222410696T^3 + 2.06254356E^{-6}T^4 \quad (3.2)$$

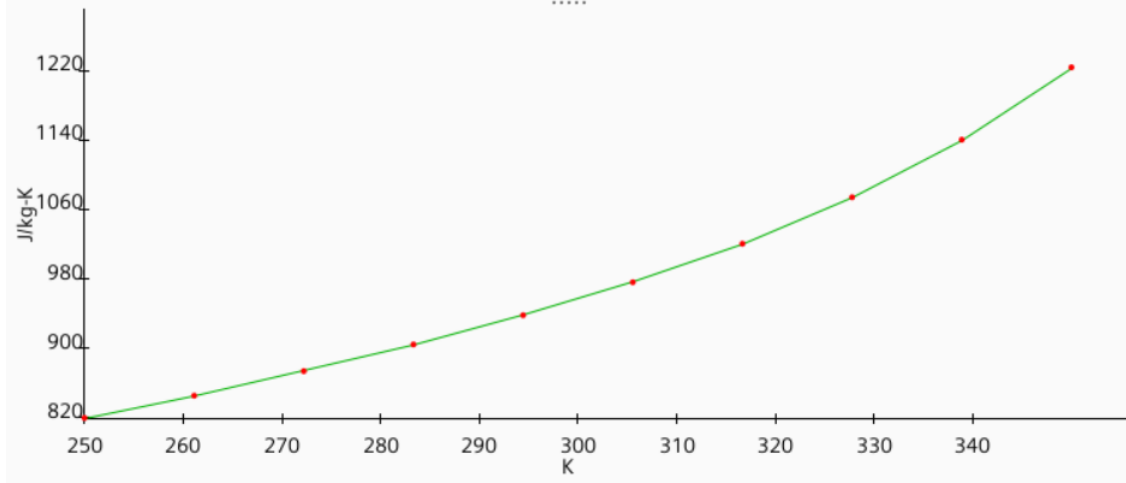


Figure 3.6: Variation of c_p as a function of temperature.

The c_p value plotted as a function of temperature which is from the above equation.

The thermal conductivity equation (λ) [W/m · K]

$$- 1.58695E^{-1}T^0 + 1.68882E^{-3}T^1 - 5.79718E^{-6}T^2 + 6.94494E^{-9}T^3 \quad (3.3)$$

These values are entered to the Star-CCM+ Material Database option. Then later selected as the gas to be used as the working fluid.

3.3 Grid independence study

A grid independence study was performed for the simulation model and 3 different mesh cases were considered which are given below,

	Coarse	Base	Fine
Inlet	2.163x10 ⁵	2.373x10 ⁵	2.607x10 ⁵
Impeller	4.212x10 ⁶	4.98x10 ⁶	5.77x10 ⁶
Diffuser	2.392x10 ⁵	2.65x10 ⁵	3.005x10 ⁵
Total	4.98x10⁶	5.85x10⁶	6.745x10⁶

Table 3.2: Number of mesh elements and their split-up.

The difference between each case is approximately one million mesh elements between them. These results are then plotted against each other to observe the difference between them. For the inlet and the diffuser case, the mesh is increased by almost 10% for every case and for the impeller part the mesh is increased by approximately 15-20%. The reason why impeller mesh is increased by a higher value is that it is the main region of focus and also the region where the flow undergoes various changes in properties and sometimes the change in properties happen drastically past a shock wave present at the leading edge of the blades. Compared to

the impeller region, the inlet region is relatively stable as the flow does not undergo any change in its properties.

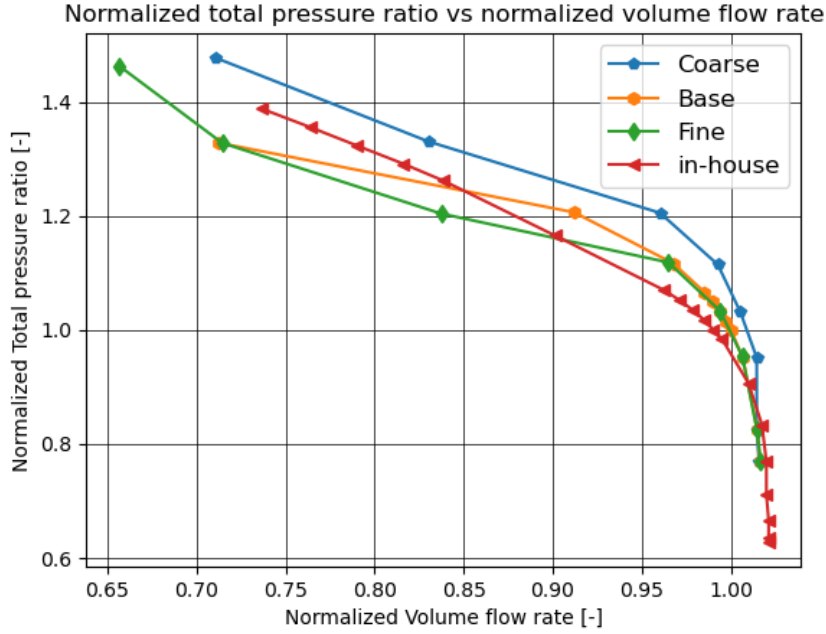


Figure 3.7: Volume flow rate vs total pressure ratio plotted for different mesh cases.

It can be seen from Figure. 3.7 that the total pressure ratio and volume flow rate of fine and base mesh cases are almost overlapping each other starting from the choke region (high volume flow rate region) until the pressure ratio of almost 1.1. The total pressure ratio of 1.0 corresponds to the design point pressure ratio. It can also be observed that for the coarse mesh case, the value of total pressure ratio is higher than the other two cases for the given volume flow rate starting choke region. Since the surge region consists of reversed flow inside the compressor, the results obtained in the surge region need more analysis. In this case, the total pressure ratio value of 1.4 was close to the numerical surge region which could explain the strange behavior seen in the curves near that region. The total pressure ratio values are obtained by varying the static pressure by a fixed value at the outlet boundary for each operating case, but the total pressure at the outlet boundary corresponding to the static pressure need not increase by a fixed value and that is obvious in the high total pressure ratio region where in the base case switching from total pressure ratio of almost 1.2 to almost 1.35 the volume flow rate drops significantly. This could indicate that the compressor is experiencing numerical surge in this operating condition.

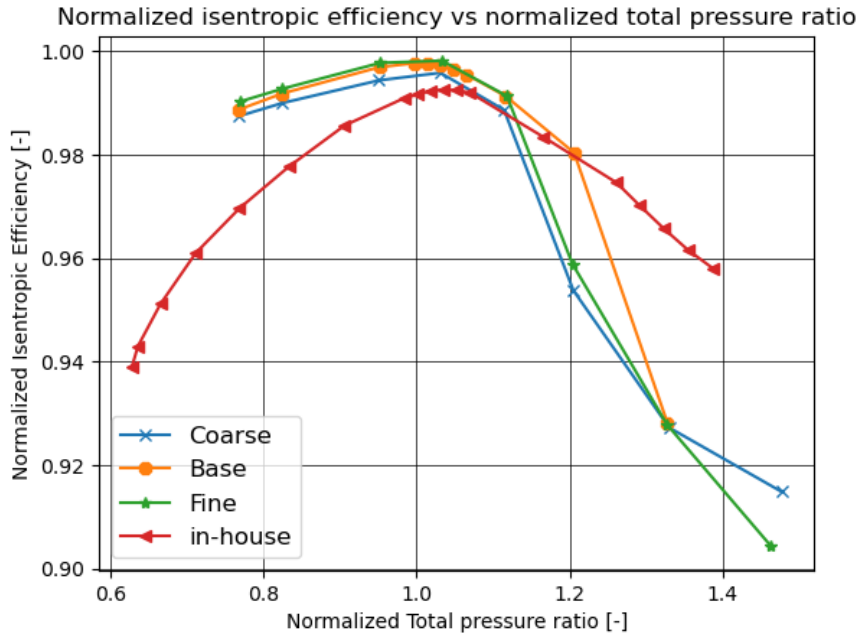


Figure 3.8: Total pressure ratio vs isentropic efficiency plotted for different mesh cases.

In the Figure 3.8, the difference between the base mesh and the coarse mesh is quite clear while the difference between the base mesh and the fine mesh was again smaller. As mentioned in the appendix A, for the base case, the surge region is close to the pressure ratio of 1.4 and the same also is true for other mesh cases which is seen clearly in the Figure. 3.7 where the volume flow rate drops drastically as the pressure ratio rises above 1.2. The efficiency values of these surge region pressure ratios are also seen to have strange behaviour and the reason the base case is not considered after the pressure ratio of approximately 1.3 is that the results in that region are not trustworthy. For the other two mesh cases, the values are depicted to have an idea of the difference between them. For the extended plot of the base case, please refer the appendix A. The difference between the isentropic efficiency values at values close to the design point for the base and coarse mesh was found to be 0.12% and for the case of base and fine mesh, the difference was found to be 0.09%. There are different operating conditions for a compressor but the design point is considered for comparison as it is in the region of focus.

3.4 Comparison between internal interface and mixing plane interface

In the chapter 3.1.3, the physics setup of the simulation are discussed and it is mentioned that the interface between the impeller and the diffuser is set to be an internal interface. To compare the difference between the internal and the mixing plane interface, a simulation case was setup with similar operating conditions but the impeller-diffuser interface was modeled as a mixing plane interface.

The difference is clearly visible between the Figure. 3.9 and 3.10, where the shock generated at the trailing edge of the blade is clearly visible in the interface boundary in the latter figure and the discontinuity travels across the diffuser while the Mach number values are averaged in the former figure. This is expected as the mixing-plane interface is not suited for this simulation as it averages the data circumferentially which makes the values on the boundary very smooth. This type of averaging is more suited for interfaces in-between two stages of a turbomachine. Hence in the further simulations, only the internal interface is considered and the mixing plane interface is not considered.

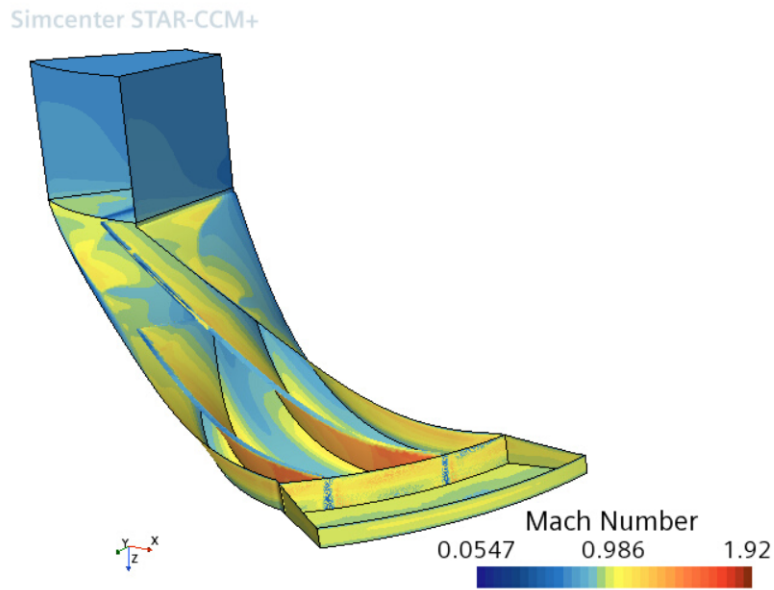


Figure 3.9: Mixing plane interface between impeller and diffuser.

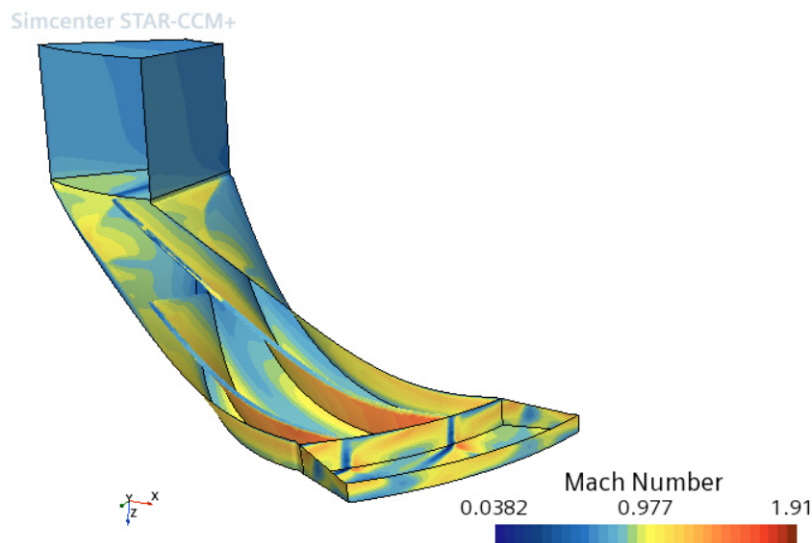


Figure 3.10: Internal interface plane interface between impeller and diffuser.

4

Results

The grid independence study is performed in the chapter 3.3 from which the base mesh is selected. After which the boundary conditions are setup and the interfaces are set according to the previous chapter 3.1.3 and chapter 3.4 results.

With the models set and the meshing complete the simulations are performed and the results from the simulations are discussed in the following order,

- First, the isentropic efficiency equation is studied and the results from that are used for further simulations.
- Second, the polytropic and isentropic efficiency of the compressor are plotted. To have an idea about both the efficiencies for this compressor.
- Third, the sensitivity study for the turbulence models are performed and used for further simulations.
- Fourth, the real gas models study is performed and the results are analysed.
- Finally, the contour plots of relative Mach number at different spanwise locations inside the compressor for different operating conditions are analysed.

The data presented here are normalized with a reference value in order to conceal the true values.

The in-house results are neither accurate nor the true ones. Hence it should be used as just a reference or an estimate of where the results are expected. The aim of the simulations were not to match the in-house results but rather use that as a reference as mentioned above.

4.1 Isentropic efficiency study

In this section the difference between the isentropic efficiency generated by the equation 2.19 taken from (Denton J., 1993) [25] and the equation 2.7 whose value is directly obtained from Star-CCM+.

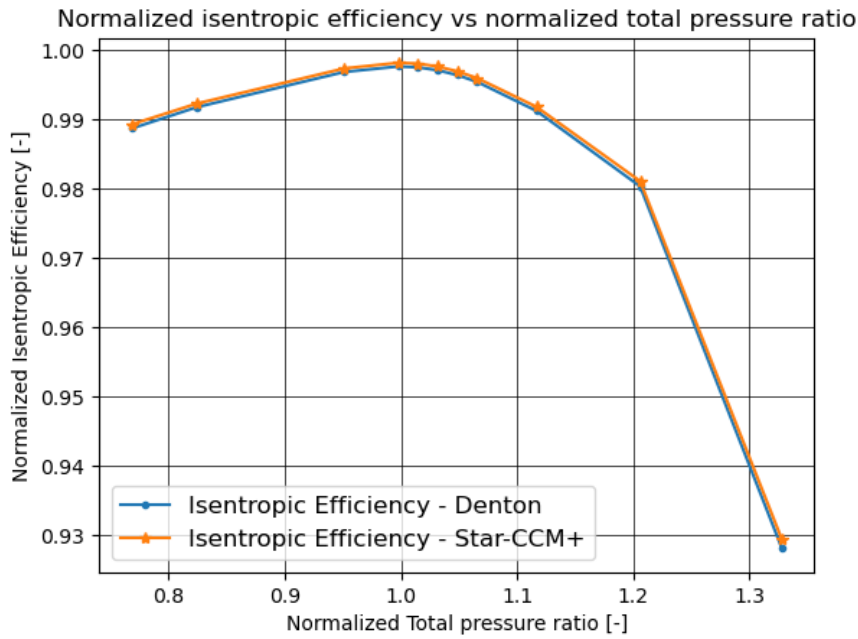


Figure 4.1: Difference between the isentropic efficiency generated by Star-CCM+ and Denton formula.

It is seen in Figure 4.1 that the values are almost identical for both the efficiencies and this shows that the the 2.19 is well suited for this process involving real gas simulation in a centrifugal compressor.

The two results are almost identical to each other because of the absence of direct usage of γ or specific heats in the equation. Since the specific heat varies as a function of temperature according to the equation in the chapter 3.2, the right way to use the property would be to calculate the value at the specific boundary and use it for the calculation of enthalpy.

4.2 The polytropic and isentropic efficiency

According to (Casey, M. 2021) [8], for an efficiency to be calculated in a reversible machine the ideal thermodynamic process has to be defined and this is where the difference between the polytropic and isentropic efficiency arises.

For isentropic efficiency it is chosen to be an ideal reversible process at constant entropy as the ideal machine has no heat transfer and losses. For the polytropic efficiency, ideal process is a reversible process whose static state coincide with the change of state of the gas in the compressor from inlet to outlet, (Casey, M. 2021) [8]. It is because of this reason that the polytropic efficiency is higher than the isentropic efficiency.

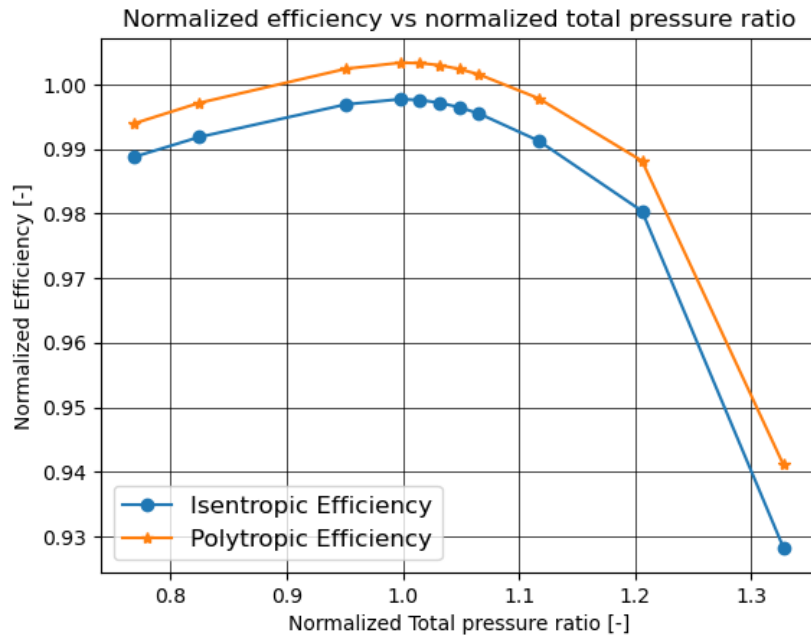


Figure 4.2: Difference between polytropic efficiency and isentropic efficiency plotted.

The isentropic efficiency is obtained from the equation 2.19 and the polytropic efficiency is obtained from the equation 2.20. In the Figure 4.2, the same trend is observed, the polytropic efficiency being higher than the isentropic efficiency. It can be observed that the change in efficiency value is very small and that the difference remains almost constant until the total pressure ratio of 1.2. After which the difference reduces and finally the difference increases to a higher value.

4.3 Turbulence model study

The next step was to change the turbulence model and to record the values. Four different turbulence models were considered for testing. First model was $k-\omega$ SST, which was considered as it is widely considered for turbomachinery applications (Menter, F., 2009) [33] and (Shah et al.) [34]. Other three models were the Realizable $k-\varepsilon$ two layer, Lag EB $k-\varepsilon$ and the Reynolds Stress Turbulence model.

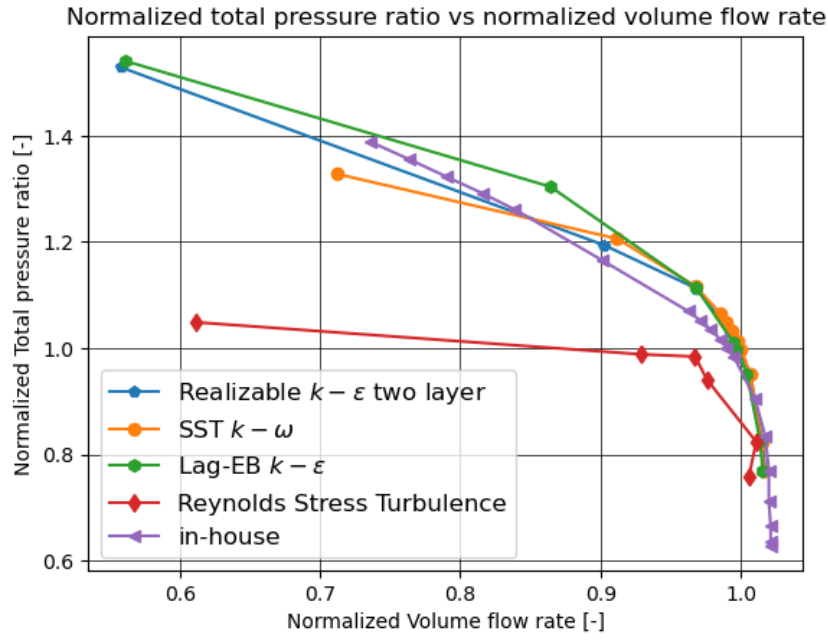


Figure 4.3: Volume flow rate vs total pressure ratio plotted for different turbulence model cases.

It can be seen in the Figure 4.3 that the behavior of the curves are similar for the case of $k-\omega$ SST, Realizable $k-\epsilon$ two layer and Lag EB $k-\epsilon$ which seem to overpredict the volume flow rate for a given total pressure ratio when compared to the in-house result. The over-prediction is quite clearly visible after the design point total pressure ratio of one, until which the values are almost coinciding. In the choke region, the maximum volume flow rate through the compressor is lower than the in-house result for all turbulence cases. This behavior is not seen in the Reynolds Stress Turbulence model as it starts with almost same values of volume flow rate for a given total pressure ratio, but then under-predicts the volume flow rate completely. This makes it easy to discard the Reynolds Stress Turbulence model.

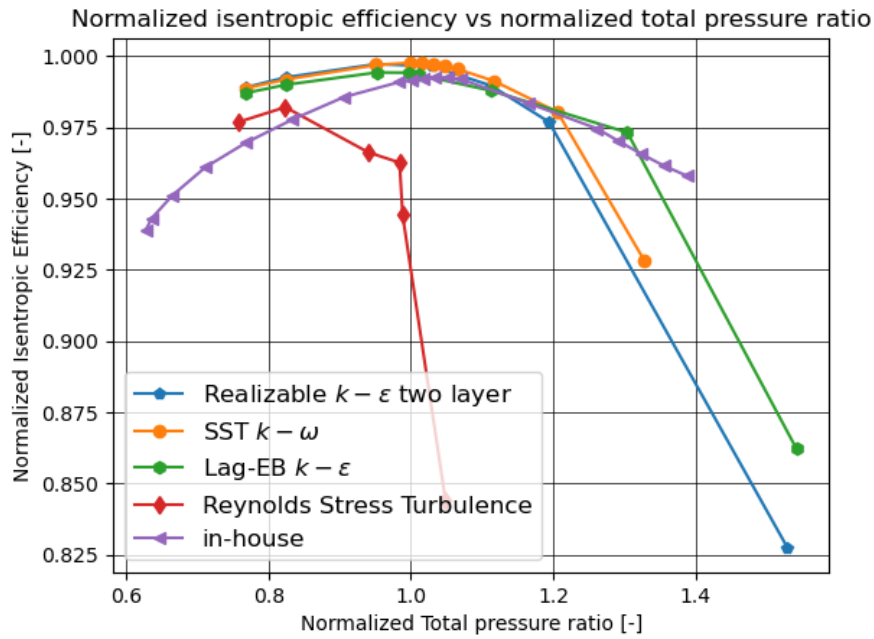


Figure 4.4: Total pressure ratio vs isentropic efficiency plotted for different turbulence model cases.

In the Figure 4.4, the observed trend of the turbulence models are similar to the results produced by the in-house software. But it is quite clear that the simulation models for all the cases seem to have a higher value of efficiency than the in-house result near the low total pressure ratio region (choke region) and near the design point. The difference between the efficiency values seem to reduce as the total pressure ratio increases and becomes almost same just past the design point. Reynolds Stress Turbulence model has a good trend near the choke region (low volume flow rate - low total pressure region) similar to the other models, but starts deteriorating after the pressure ratio of 0.8.

The way the turbulence models match the in-house result in terms of the maximum efficiency observed at the design point, shows that the computational model set up to the study the flow through the centrifugal compressor using the RANS equation is acceptable and that the field functions are defined properly within the solver.

The behavior of $k-\omega$ SST and Realizable $k-\epsilon$ two layer are quite similar with respect to the in-house. Their trend stays the same until the pressure ratio of 1.2 after which the $k-\omega$ SST seems to behave inconsistently which can be attributed to the surge region which makes the flow behavior unpredictable and hence drops the efficiency of the compressor. But in Realizable $k-\epsilon$ two layer the trend seems to continue further down in the same direction. The $k-\omega$ SST is almost almost 0.04% higher in value when compared to Realizable $k-\epsilon$ two layer at the design point and it is the other way around for the volume flow with $k-\epsilon$ two layer higher by $0.05 \text{ m}^3/\text{s}$ than $k-\omega$ SST at the design point.

Lag EB $k-\epsilon$ also has a very similar nature in the trend but it follows the in-house

result much further past the 1.2 pressure ratio region, way past the design point pressure ratio. This shows that the Lag EB $k-\varepsilon$ has seemingly better performance when compared to the other turbulence models.

4.4 Gas models study

The next step was to select the real gas model suitable for the simulation. Real gas is selected during the setup of the physics of the simulation. Inside the real gas option, there were a lot of options to model the real gas behavior. Basic real gas equation is based upon the Van der Waals equation which tries to include the effect of interaction between the molecules of a gas in the ideal gas equation. The Redlich-Kwong equation is very similar to Van der Waals with only a slight modification made to the attractive term. Redlich-Kwong is one of the accurate two equation system to model the behavior of real gas with very good accuracy. Other models like Soave Redlich-Kwong, Peng-Robinson were modifications performed on the Redlich-Kwong equations. More about these models were discussed in Chapter 2.5.

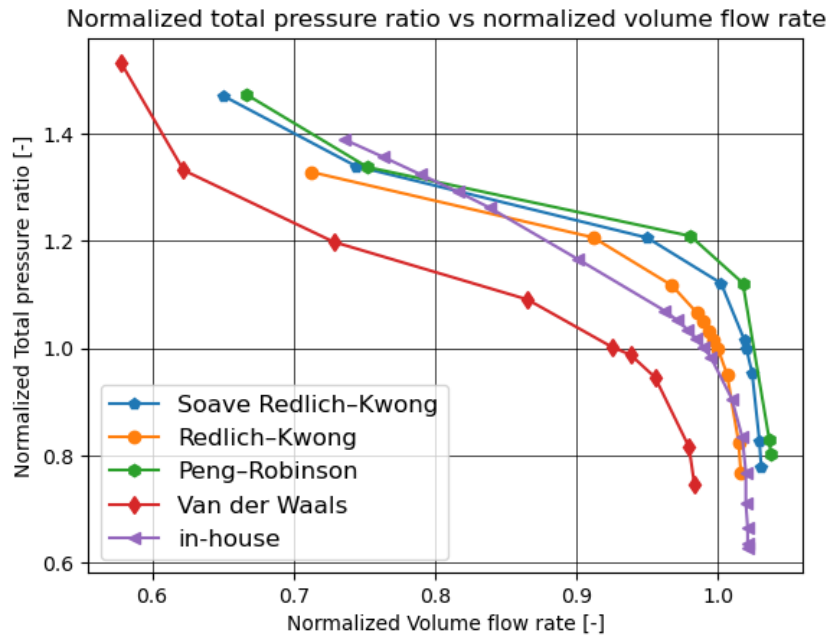


Figure 4.5: Volume flow rate vs total pressure ratio plotted for different real gas model cases.

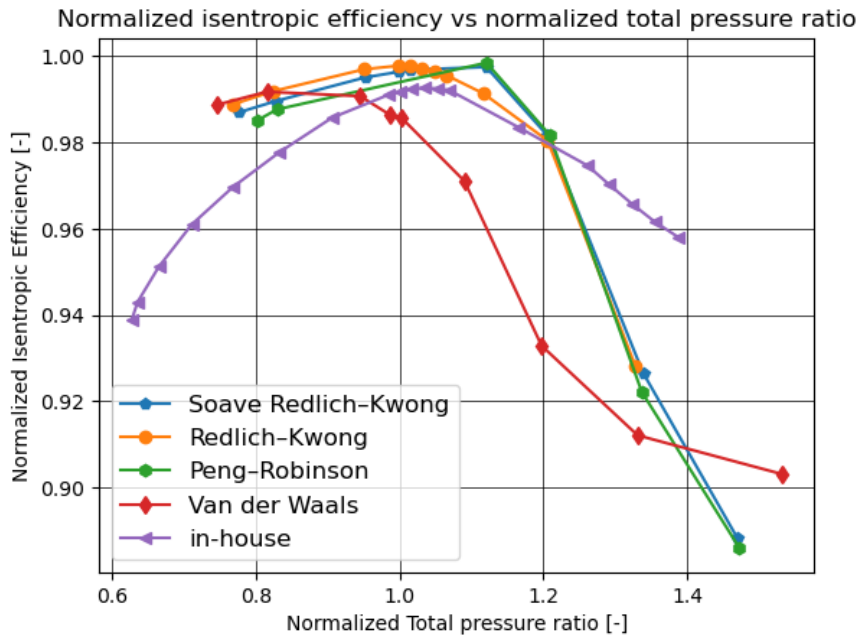


Figure 4.6: Total pressure ratio vs isentropic efficiency plotted for different real gas model cases.

In the Figures 4.5 and 4.6, the effect of modification of the real gas models are studied and plotted. In the Figure 4.5, the difference between each models is clearly visible even though the trend depicted by the models are similar to the in-house model. It is clear that in the choke region, the models seem to have higher volume flow rate when compared to the in-house model. The Redlich-Kwong model has values which are close to the in-house values starting from choke region to the design point, after which it starts deviating. The other models are have higher values in the choke region, design point but are almost at the surge region.

Van der Waals model as a real gas model was not chosen as its modeling of real behavior is not sufficient for many applications and was not widely used after the derivation of other formulas, but it was also chosen in order to observe the difference the other models and this, since this model is quite simple in terms of its modeling, it is unable to produce acceptable results.

In the latter Figure 4.6, near the design point pressure ratio, the value of efficiency for the Redlich-Kwong, Peng-Robinson and the Soave Redlich-Kwong models is close to that of the in-house results. After the pressure ratio of 1.0, the Peng-Robinson and Soave Redlich-Kwong model have an identical trend and have almost same values. But the Redlich-Kwong model is closer to the in-house result. When compared in terms of maximum value of efficiency, it can be observed that for the Redlich-Kwong case, the maximum efficiency is at the design point same as the in-house case, but that is not the case in the other models. In the Soave Redlich-Kwong and Peng-Robinson model, since the maximum efficiency is after the design point, it depicts the compressor to have a higher surge margin, which is not the case. Hence, the Redlich-Kwong model can be given the first preference when selecting gas model

for such simulations.

The Van der Waals has same value as other models in the choke region but after the pressure ratio of 0.8, its value drops down significantly leading to it having a completely different trend when compared to others.

4.5 Effect of diffuser in the compressor

The role of the diffuser in a compressor is discussed in chapter 2.3. Where the main task of the diffuser is to convert a portion of the remaining kinetic energy into static pressure rise. In general diffuser also entails some incidence losses and friction losses but in this case of vaneless diffuser, there cannot be incidence losses as there are no vanes to obstruct the flow. Hence when compared to vaned diffuser in a compressor, the vaneless diffuser has lower peak attainable efficiency.

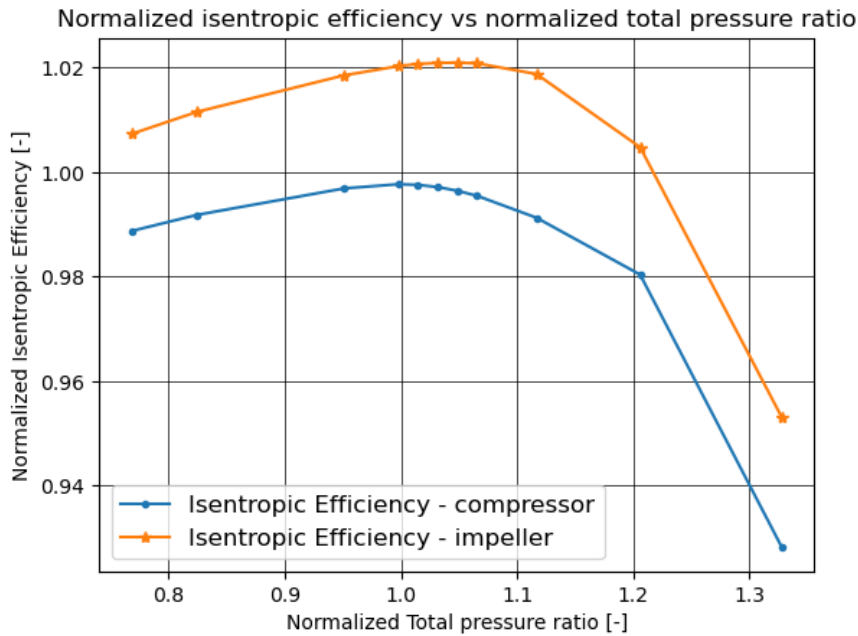


Figure 4.7: Comparison between isentropic efficiency of a compressor and of an impeller.

In the Figure 4.7, it is clear that the efficiency of a compressor without a diffuser with just inlet and impeller is higher than that of the same compressor with the diffuser. It is shown in (Doustmohammadi, A, 2013) [35] where the impeller efficiency is the highest then followed by the diffuser efficiency and then the overall compressor efficiency.

Also in (Doustmohammadi, A, 2013) [35], it is shown that the loss generated by the impeller is much higher than the diffuser for a given value of flow coefficient and the value increases as the RPM of the compressor increases. With that said, it is also shown that the contribution to the compressor efficiency reduction is also the

highest by the impeller which contributes to more than half of the reduction in a compressor for a given RPM. The contribution increases as the RPM increases for the impeller, but it remains more or less constant for the diffuser.

In low RPM conditions in the compressor, the main loss in the impeller is due to incidence loss and as the mass flow rate increases, the incidence loss decreases as the difference between the flow relative angle and the blade angle reduces (Doust-mohammadi, A, 2013) [35]. For diffuser it is vice versa, the losses increases as the mass flow rate increases.

4.6 Analysis of flow characteristics inside the compressor

Here, the relative Mach number contour plot is plotted for three operating conditions at three spanwise locations in order to achieve a clear idea about the flow characteristics inside the compressor.

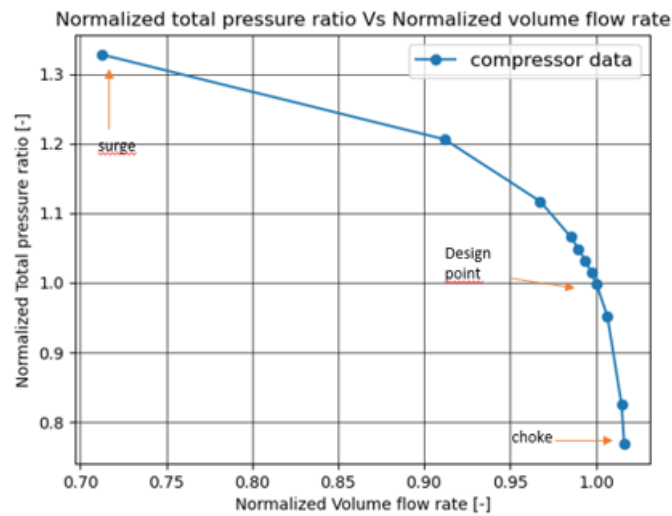


Figure 4.8: Compressor characteristic curve showing the operating point considered for analysis.

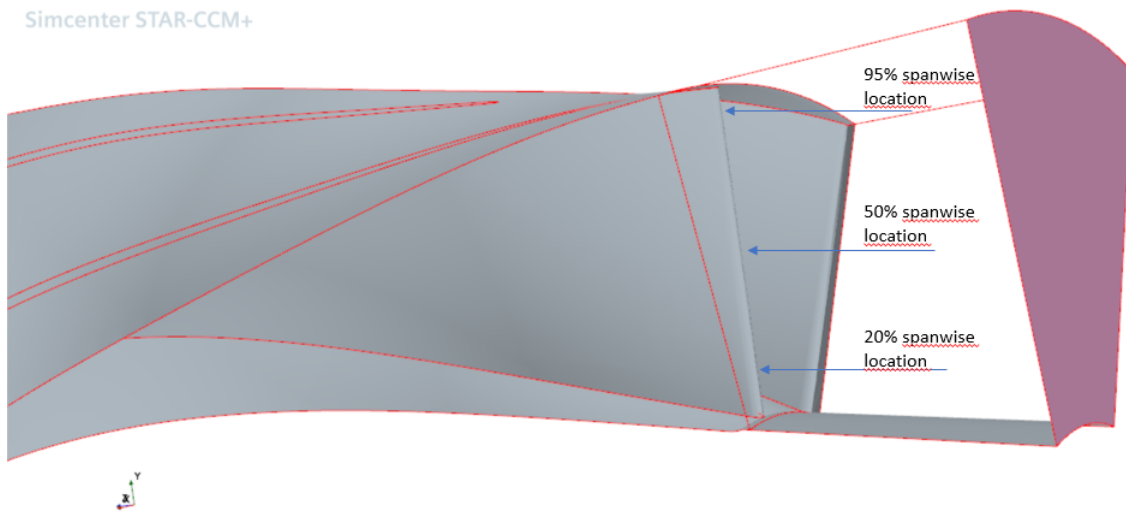


Figure 4.9: 20%, 50% and 95% spanwise locations indicated as selected for analysis.

4.6.1 Design point analysis of compressor

The two-dimensional analysis of the compressor is done in this chapter and here the main aim is to visualize the flow through the main gas path and to check for abnormal or strange behaviour.

First looking at the design point relative Mach contour plot, in Figure 4.10 it can be observed clearly the presence of supersonic flow at the LE of the main blade. The highest value is attained at the LE and the value reduces to subsonic levels after that. Moving towards the TE, the presence of a shock starting from the main blade and leading into the diffuser is observed. It appears to be a strong shock as the Mach number behind the shock reaches low subsonic levels. Behind the TE of the splitter blade there is also a sharp drop in relative Mach number, which could be due to the wake region behind the body. The wake from both the blades are seen towards the edge of the diffuser and does not affect the diffuser flow significantly.

Looking next at Figure 4.11, one can clearly see that the maximum value of relative Mach is observed at the LE of the main blade and also the region of high relative Mach is bigger than the previous figure. The relative Mach number from the LE of the main blade to the LE of the splitter blade is subsonic which might suggest that there is a LE shock originating from the main blade and in the direction of the splitter blade. This shock could affect the flow between the main blade and the splitter blade. It also looks like there is supersonic flow at the LE of the splitter blade and the but the flow becomes subsonic very quickly. It is also quite evident that a significant portion the flow in the diffuser is supersonic which are mildly separated by the shock waves from the main blade. The subsonic wake from the main blade starts as a thin layer and widens slowly as it reaches the diffuser exit.

Finally looking at the flow near the tip of the blade Figure 4.12, the shock wave

between the main blade and the splitter blade is quite clearly visible now and it looks like an oblique shock wave and the angle has changed from the previous case. The compressor and blade have a three-dimensional profile and hence flow must also turn in the side of the suction surface, which might be one of the reasons for the shock to change angle and direction. There is also a region of low velocity flow observed in between the main blade and the splitter blade and this can be attributed to the curvature of the impeller which is larger at the tip than at the hub and this in turn leads to a larger adverse pressure gradient which leads to thickening of the boundary layer at that location (Sundström, E, 2017) [36]. Also at the diffuser region, the shock seems stronger than the shock observed at the LE of the blades. The value of relative Mach drops to very low values and it continues flow in the wake region in between the supersonic flow surrounding it.

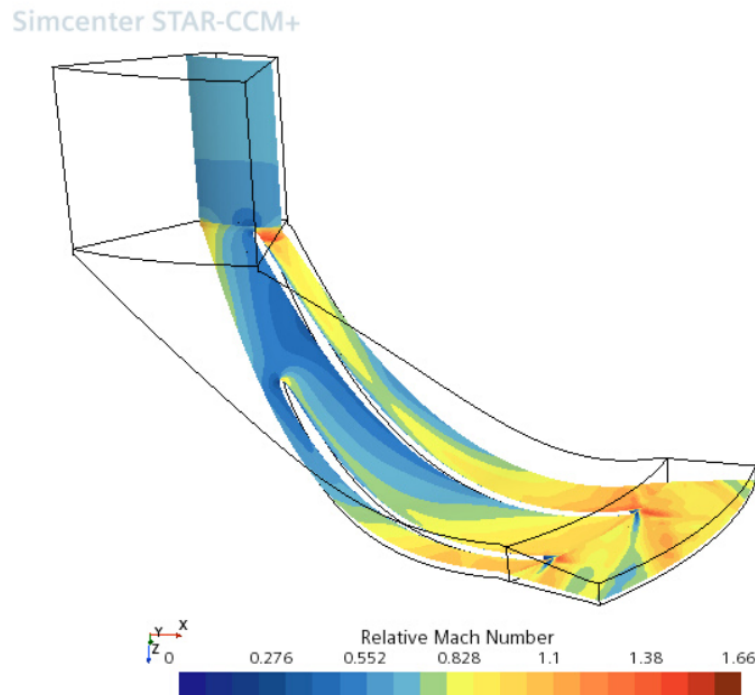


Figure 4.10: Analysis of relative Mach number at the inlet, impeller and diffuser at 20% spanwise location for design point operating condition.

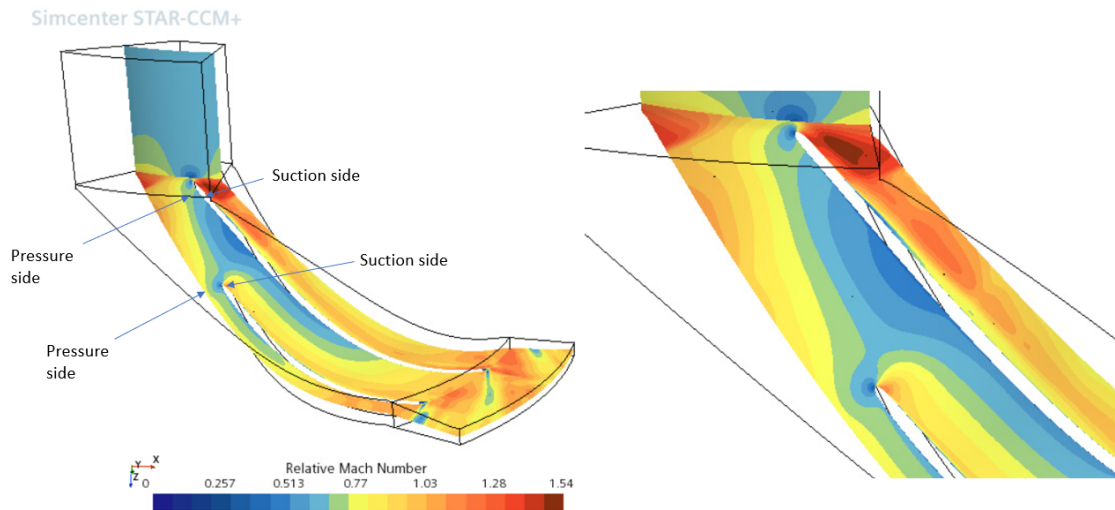


Figure 4.11: Analysis of relative Mach number at the inlet, impeller and diffuser at 50% spanwise location for design point operating condition.

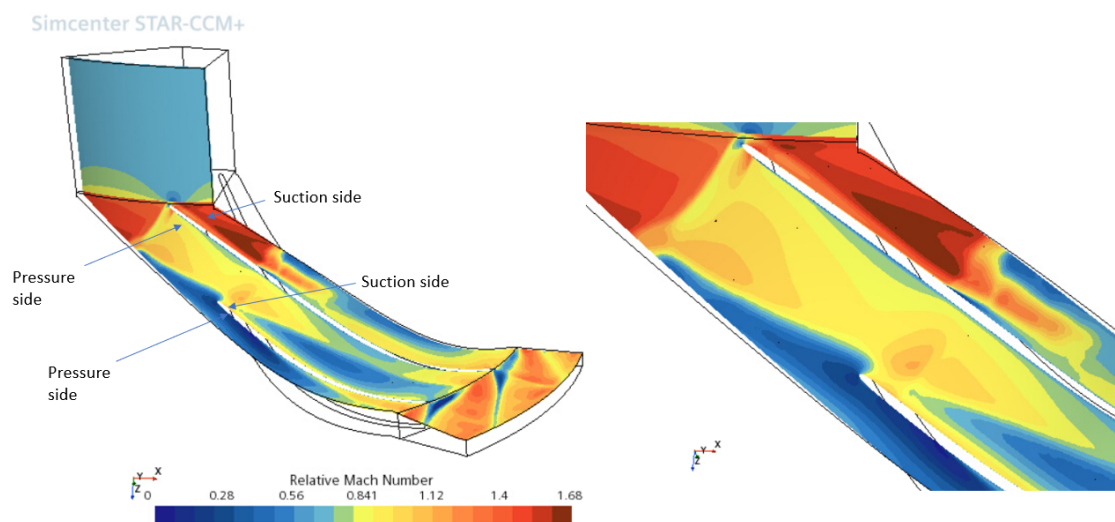


Figure 4.12: Analysis of relative Mach number at the inlet, impeller and diffuser at 95% spanwise location for design point operating condition.

4.6.2 Off-design operation analysis

The analysis of a compressor at the design point is extremely important, but having knowledge and information about how the flow behaves in off-design is even more important. This is because the compressor performance and the stress/force experienced by the blades are severely affected when operated at such dangerous conditions. The Figure 4.8 shows the points selected for the off-design analysis.

4.6.2.1 Choke region

The choke operating region is low pressure ratio and high mass flow rate through the compressor region. Since the pressure ratio is low, the fluid is not as compressed

when compared to its higher pressure ratio counterparts. Hence the behavior of fluid inside the compressor is significantly different from other cases.

Looking at the Figure 4.13, it is seen that the maximum Mach is achieved at the LE of the main blade similar to the design point Figure 4.10, with the main difference in the flow behavior originating in the diffuser where the wake region is quite well established in the design point when compared to this case.

Looking at Figure 4.14, it is almost exactly identical to the Figure 4.11 when comparing the flow from the inlet to the midspan of the blade. But when coming towards the TE and the diffuser region, it can be seen clearly that the higher relative Mach number is observed in this case. When looking back at the theory of centrifugal compressors, the main job of the diffuser is to convert the kinetic energy into static pressure. As given in this velocity diagram Figure 2.8, it is seen that the relative velocity of the fluid reduces which is in turn converted into static pressure rise. Now since the relative velocity is high in this case, it can be said that the diffuser did not reduce the relative velocity as effectively when compared to the design point case.

Looking at the same Figure 2.8, it can be seen that the absolute velocity of the flow increases as it exits the impeller, which implies that the absolute Mach number should be higher than the relative Mach number for a given operating case except the surge region, which is shown in Appendix C.

Coming to the tip flow in Figure 4.15, the it is once again clear that this case is very similar to the Figure 4.12 starting from the inlet and also has a similar position of oblique shock waves at the LE of main blade and splitter blade and also having shock at the TE of the blades. Though it can be said that the strength of shock wave at the LE of the main blade is not as strong as the Figure 4.12 case where the flow becomes subsonic after the shock whereas that is not the case here. Another difference is the region of low mass flow in between the blades which is small in this case and this could be due to the strength of adverse pressure gradient being lower than the Figure 4.12 case. The main difference arises again in the wake region in the diffuser part. The wake is wider in this case when compared to Figure 4.12 and which could be attributed to the mass flow rate through the compressor as the diffuser loss increases as the mass flow rate increases.

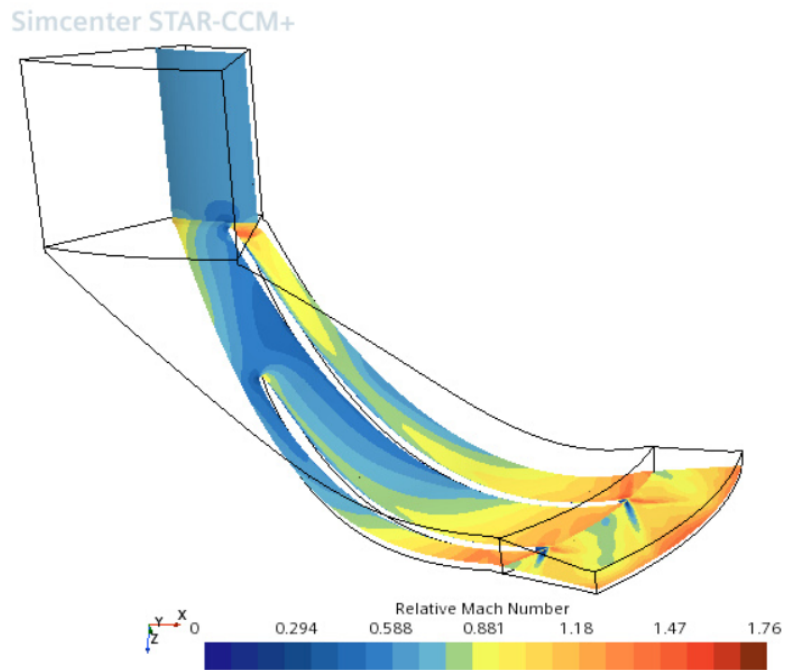


Figure 4.13: Analysis of relative Mach number at the inlet, impeller and diffuser at 20% spanwise location for choking region operating condition.

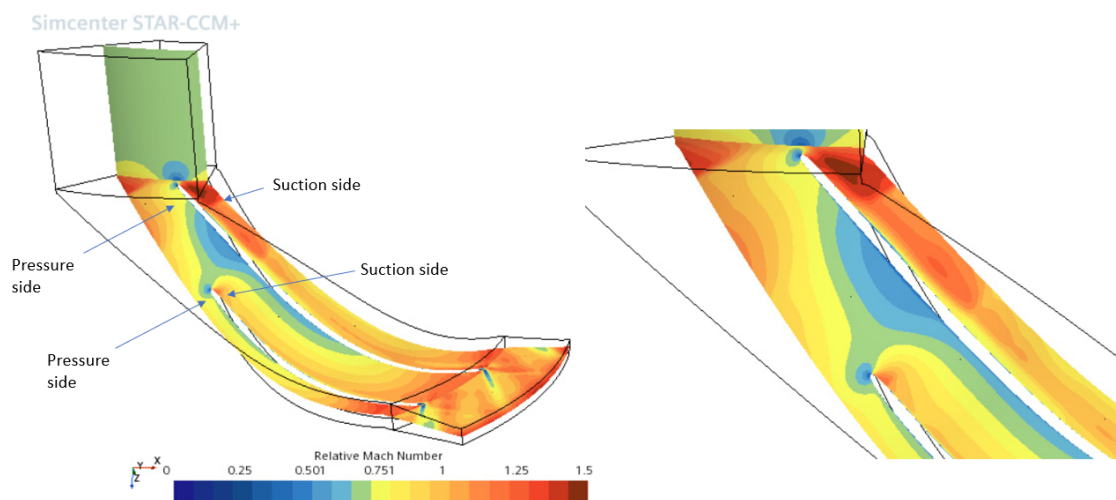


Figure 4.14: Analysis of relative Mach number at the inlet, impeller and diffuser at 50% spanwise location for choking region operating condition.

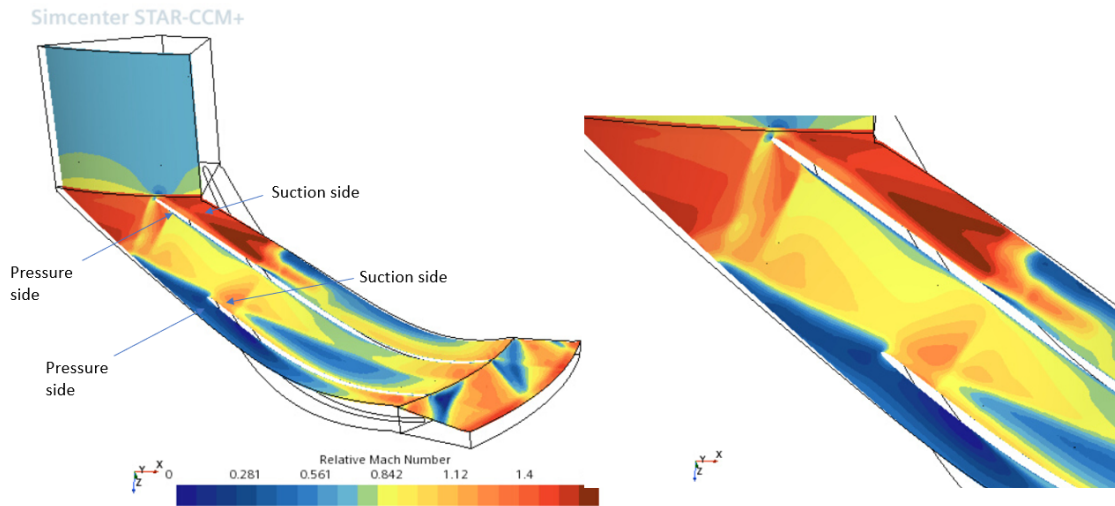


Figure 4.15: Analysis of relative Mach number at the inlet, impeller and diffuser at 95% spanwise location for choking region operating condition.

4.6.2.2 Surge region

The surge region is defined by the low mass flow rate and high pressure ratio which is quite inverse of the previous case discussed. The flow behavior in this section is extremely unpredictable and the compressor should not be operated in this condition for long periods.

Looking at the Figure 4.16, the flow pattern is completely different from its design point counterpart Figure 4.10. Though the maximum relative Mach reached is higher in this case, the region of high Mach is very small at the LE of the main blade. The region in between the main blade is fully subsonic like its counterpart. But the flow in the diffuser section is distinctly different. The relative Mach is observed to be subsonic for most of the region and the wake from the blades are wide when compared to Figure 4.10 where the flow is supersonic in most of the diffuser.

Looking at the Figure 4.17, the flow is supersonic at the LE of the main blade whose region is longer than the region observed in the Figure 4.11. The flow in between the blades seems to be almost choked. Looking at the diffuser section, it is clear that the flow seems more tangential than in the Figure 4.11 which could be said from the angle of the wake behind the blades. The flow is supersonic with a higher value for the most part of the diffuser, so it could suggest that the diffuser is not efficient at this operating condition. Since the efficiency of the compressor in this region is lower than the design point case, it could be from the fact that the diffuser is unable to reduce the relative velocity to a greater extent.

Comparing Figure 4.18 and Figure 4.12, it is seen that the flow is behaving in a completely different and in an unexpected manner. The low Mach region in almost all the region in the impeller could be due to the stronger adverse pressure gradient which causes the flow separation to be much prevalent and thereby affecting the

4. Results

performance. The flow is supersonic at the diffuser in most parts except for the subsonic wake from the blades.

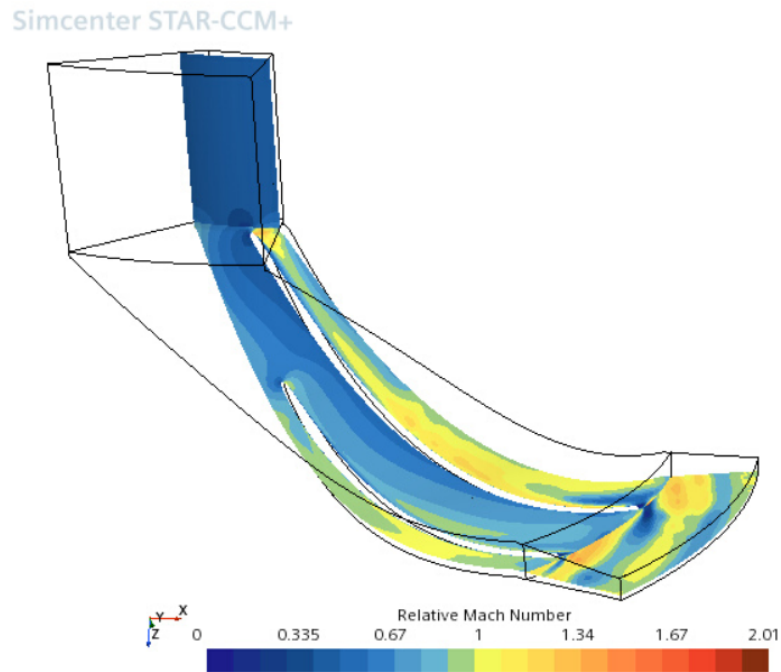


Figure 4.16: Analysis of relative Mach number at the inlet, impeller and diffuser at 20% spanwise location for surge region operating condition.

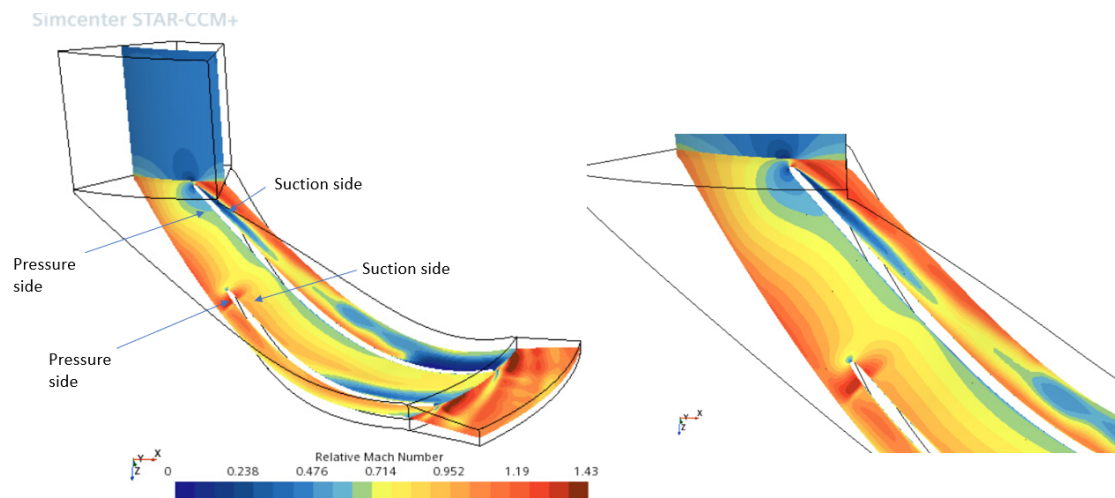


Figure 4.17: Analysis of relative Mach number at the inlet, impeller and diffuser at 50% spanwise location for surge region operating condition.

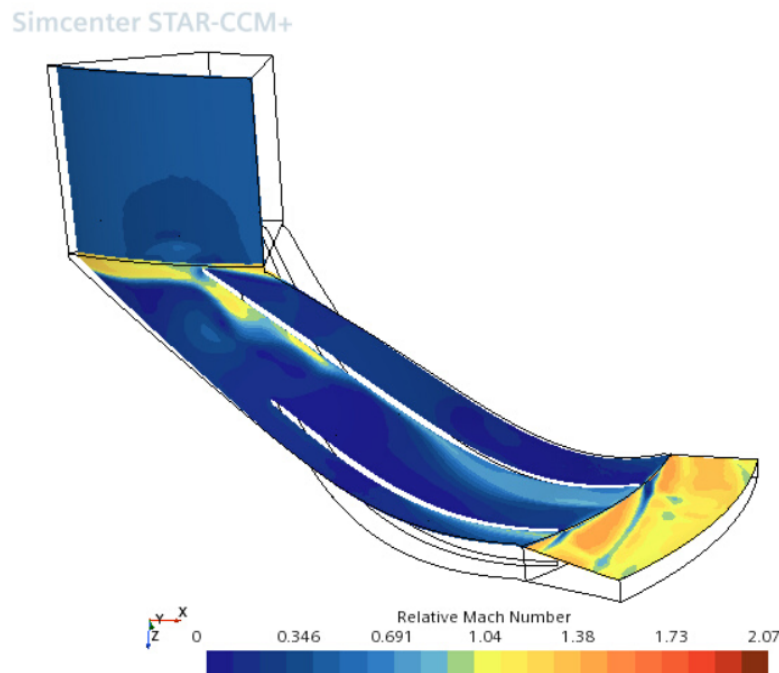


Figure 4.18: Analysis of relative Mach number at the inlet, impeller and diffuser at 95% spanwise location for surge region operating condition.

4.7 Comparison of results between Star-CCM+ and ANSYS CFX

In this section the results between the CFD software and ANSYS CFX is compared. The simulation setup in the CFX software was as follows,

- The turbulence model is $k-\epsilon$. Which is also widely used for turbomachinery applications.
- The real gas model used was Aungier Redlich-Kwong which is also a modification of the Redlich-Kwong model like Peng-Robinson and Soave Redlich-Kwong.
- The number of mesh elements was approximately 3.7M elements.

With the basic information about the setup known, it is clear that the simulation setup is similar to this work. Hence the results from the simulation of ANSYS CFX with the above given setup can be compared with the Star-CCM+ results. The comparison plots are shown below.

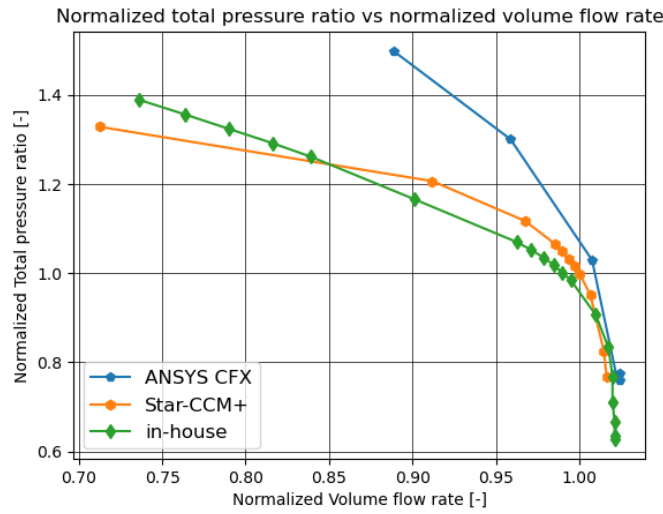


Figure 4.19: Volume flow rate vs total pressure ratio plotted for Star-CCM+ and ANSYS CFX.

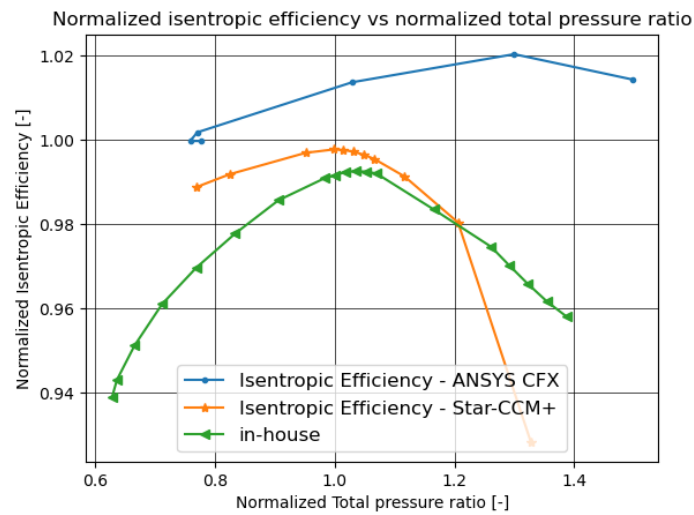


Figure 4.20: Total pressure ratio vs isentropic efficiency plotted for Star-CCM+ and ANSYS CFX.

In high surge regions the the pressure and mass flow oscillates within the compressor and these oscillations create noise, negatively affects the performance and can also damage the compressor. In simple terminology, the compressor surge margin defined as,

$$SM = 100 \cdot \frac{PR_{\text{surge}} - PR_{\text{operatingline}}}{PR_{\text{operatingline}}} = 100 \cdot \left(\frac{PR_{\text{surge}}}{PR_{\text{operatingline}}} - 1 \right) \quad (4.1)$$

With the above definition, it can be seen in Figure 4.20 that the expected design point ratio is at 1.0, the difference between the surge pressure ratio and this is very large for CFX than Star-CCM+ which could mean the compressor is not designed

properly. It can also be seen in the same figure that the value of maximum isentropic efficiency is almost 2% higher for CFX than the value obtained by Star-CCM+.

The Figure 4.19, which has the total pressure ratio and the volume flow rate, show that the volume flow rate through the compressor in CFX is much higher than the other two cases. It is worth noting that the choked volume flow rate value between Star-CCM+ and the CFX is almost similar.

5

Conclusion

The simulations were performed for the centrifugal compressor with R1234ze(E) as the working fluid using the Star-CCM+ software. The aim was to develop the process of setting up and performing the simulation of a centrifugal compressor in Star-CCM+ using R1234ze(E) as the refrigerant. Then to evaluate the performance of the compressor.

It started from the process of acquiring the geometry and converting the base file to necessary input files and making some changes in order to ensure smooth preparation of the geometry. The geometry was then meshed according to the results from the grid independence study. Then the necessary physics models were setup and the simulations were performed. Thereafter switching different turbulence models and different gas models which were suitable for this type of operation were performed.

The results from the simulation which involved testing of different turbulence models and different real gas models which are considered part of a CFD simulations procedure. In this case, since there are no predefined recommendations, the following conclusions are made from the simulations. The turbulence model which can be used for this simulations are Lag-EB $k-\varepsilon$ and $k-\omega$ SST models as the results of the simulation using those turbulence models yielded better results. In terms of the real gas models, Redlich-Kwong gas model is best suited for such refrigerants as the other models have results which have a slightly higher surge margin than expected. In terms of the interface plane between the rotating impeller region and the static diffuser region, internal interface can be used as it does not circumferentially average the data. Since the results regarding the performance of the compressor involves the isentropic efficiency, it is of critical importance that the efficiency formula is well defined and for this, the equation 2.19. Star-CCM+ also has a built-in option to generate isentropic efficiency values for the given operation and the result from this is based on the eq. 2.7 and this is in good relation with eq. 2.19. The polytropic efficiency is obtained from 2.20 and this is also independent of c_p, c_v and γ and hence there are no simplifications or averages and hence it can also be used to calculate the polytropic efficiency.

5.1 Future Work

A base has been established for performing CFD simulations for this compressor with this refrigerant, but there are things which can be improved upon and things

that can be added to this to make it more accurate and versatile.

For instance, the IGVs were not added to this setup as there was not enough time to add and perform simulations for different angles of IGV. So in the future, analysis on the effect of IGV on the compressor can be studied in detail.

The inlet part was simplified during the CAD modeling phase. It was modelled as a constant diameter section extending from the impeller inlet region with straight lines extended from hub and casing at the impeller inlet. This is not true in real case as the presence of inlet guide vanes alter the casing diameter and the hub diameter of the compressor. For this work, the inlet region was modelled to ensure that the flow entering the impeller region is uniform and to avoid reversed flow near the leading edge of the main blade.

The diffuser part was also simplified during the CAD phase where the impeller exit to diffuser entry has a filleted region for the transition which then extended till the diffuser exit. This was simplified as a straight line from the impeller exit to the diffuser exit coordinates provided.

Bibliography

- [1] Large-scale Industrial Heat Pumps;. Available from: <https://www.siemens-energy.com/global/en/offerings/power-generation/heat-pumps.html>.
- [2] Lu J, He G, Mao F. Solar seasonal thermal energy storage for space heating in residential buildings: Optimization and comparison with an air-source heat pump. *Energy Sources, Part B: Economics, Planning and Policy*. 2020;279–296.
- [3] Dincer I, Ezzat MF. 3.4 Renewable Energy Production. In: Dincer I, editor. *Comprehensive Energy Systems*. Oxford: Elsevier; 2018. p. 126–207. Available from: <https://www.sciencedirect.com/science/article/pii/B9780128095973003102>.
- [4] Ninikas K, Hytiris N, Emmanuel R, Aaen B, McMillan S. A renewable heat solution for water ingress in the Glasgow subway tunnel system. *WIT Transactions on Ecology and the Environment*. 2014;186:161–171.
- [5] Aungier RH. *Centrifugal compressors : a strategy for aerodynamic design and analysis*. ASME Press; 2000.
- [6] Dixon SL, Hall CA. Chapter 7 - Centrifugal Pumps, Fans, and Compressors. In: Dixon SL, Hall CA, editors. *Fluid Mechanics and Thermodynamics of Turbomachinery (Sixth Edition)*. sixth edition ed. Boston: Butterworth-Heinemann; 2010. p. 217–263. Available from: <https://www.sciencedirect.com/science/article/pii/B9781856177931000079>.
- [7] Gravdahl Jan Tommy }and Egeland O. Compressor Surge and Stall: An Introduction. In: *Compressor Surge and Rotating Stall: Modeling and Control*. London: Springer London; 1999. p. 1–62. Available from: https://doi.org/10.1007/978-1-4471-0827-6_1.
- [8] Casey M, Robinson C. Efficiency Definitions for Compressors. In: *Radial Flow Turbocompressors: Design, Analysis, and Applications*. Cambridge University Press; 2021. p. 106–134.
- [9] Cengel YA, Boles MA. *Thermodynamics: an engineering approach*. 8th ed. New York: McGraw-Hill Book; 2015.
- [10] Surge in Compressors;. Available from: https://en.wikipedia.org/wiki/Surge_in_compressors.
- [11] Compressor Characteristics;. Available from: https://en.wikipedia.org/wiki/Compressor_characteristic.
- [12] The pressure-enthalpy diagram;. Available from: <https://www.swep.net/refrigerant-handbook/2.-compression-cycle/zx4/>.

- [13] pierr e gregoire SM. Greenhouse Gas Emissions from Fossil Fuel Fired Power Generation Systems.; 2001.
- [14] Carbon Dioxide - Vital Signs – Global Climate Change - Vital Signs of the Planet;. Available from: <https://climate.nasa.gov/vital-signs/carbon-dioxide/>.
- [15] Wuebbles DJ. The role of refrigerants in climate change. International Journal of Refrigeration. 1994;17(1):7–17. Available from: <https://www.sciencedirect.com/science/article/abs/pii/0140700794900825>.
- [16] Werner S. District Heating and Cooling. In: Cleveland CJ, editor. Encyclopedia of Energy. New York: Elsevier; 2004. p. 841–848. Available from: <https://www.sciencedirect.com/science/article/pii/B012176480X00214X>.
- [17] Hoffmann K, Forbes D, Minstr P, Chamber L. Ammonia Heat Pumps for District Heating in Norway - a case study. The Institute of Refrigeration; 2010. Available from: <https://web.archive.org/web/20131203054940/http://www.ammonia21.com/web/assets/link/Hoffman7thApril2011London%20colour.pdf>.
- [18] Air source heat pump; 2015. Available from: <https://www.energimyndigheten.se/en/sustainability/households/heating-your-home/heat-pump/air-source-heat-pump/#:~:text=The%20outdoor%20air%20source%20heat,the%20domestic%20hot%20water%20system>.
- [19] Heat Pump;. Available from: [https://en.wikipedia.org/wiki/Heat_pump#Geothermal_\(ground-source\)_heat_pump](https://en.wikipedia.org/wiki/Heat_pump#Geothermal_(ground-source)_heat_pump).
- [20] Lund J. GEOTHERMAL HEAT PUMPS - TRENDS AND COMPARISONS. 2022 6. Available from: https://www.researchgate.net/publication/242258521_GEOTHERMAL_HEAT_PUMPS_-_TRENDS_AND_COMPARISONS.
- [21] Wilkes J, Pettinato B, Kurz R, Hollingsworth J, Zhang D, Taher M, et al. Chapter 3 - Centrifugal Compressors. In: Brun K, Kurz R, editors. Compression Machinery for Oil and Gas. Gulf Professional Publishing; 2019. p. 31–133. Available from: <https://www.sciencedirect.com/science/article/pii/B9780128146835000031>.
- [22] Turunen-Saaresti T. Computational and experimental analysis of flow field in the diffusers of centrifugal compressors /. 2004 5.
- [23] Karlsson A. Aerodynamic Design of Centrifugal Compressor for Heavy Duty Truck Applications. Lund: Lund University; 2018.
- [24] Isentropic efficiency report for a turbine/nozzle; 2019. Available from: https://support.sw.siemens.com/en-US/product/226870983/knowledge-base/KB000041696_EN_US.
- [25] Denton JD. Loss Mechanisms in Turbomachines. Mechanical Engineers; 1993. Available from: <http://asmedigitalcollection.asme.org/GT/proceedings-pdf/GT1993/78897/V002T14A001/4457435/v002t14a001-93-gt-435.pdf>.
- [26] Semlitsch B, Mihaescu M. Flow phenomena leading to surge in a centrifugal compressor. Energy. 2016;103:572–587. Available from: <https://www.sciencedirect.com/science/article/pii/S0360544216302766>.

-
- [27] Yang M, Martinez-Botas R, Zhang Y, Zheng X. Effect of Self-Recirculation-Casing Treatment on High Pressure Ratio Centrifugal Compressor. *Journal of Propulsion and Power*. 2016;32(3):602–610. Available from: <https://doi.org/10.2514/1.B35438>.
- [28] Tsonopoulos C, Heidman JL. From Redlich-Kwong to the present. *Fluid Phase Equilibria*. 1985;24(1):1–23. Available from: <https://www.sciencedirect.com/science/article/pii/0378381285870345>.
- [29] Soave G. Equilibrium constants from a modified Redlich-Kwong equation of state. *Chemical Engineering Science*. 1972;27(6):1197–1203.
- [30] Graboski M, Daubert T. A Modified Soave Equation of State for Phase Equilibrium Calculations. 2. Systems Containing CO₂, H₂S, N₂, and CO. *Industrial & Engineering Chemistry Process Design and Development*. 1978 10.
- [31] Graboski MS, Daubert TE. A Modified Soave Equation of State for Phase Equilibrium Calculations. 1. Hydrocarbon Systems. *Industrial & Engineering Chemistry Process Design and Development*. 1978;17(4):443–448. Available from: <https://doi.org/10.1021/i260068a009>.
- [32] Lemmon EW, Bell IH, Huber ML, McLinden MO. NIST Standard Reference Database 23: Reference Fluid Thermodynamic and Transport Properties-REFPROP, Version 10.0, National Institute of Standards and Technology; 2018. Available from: <https://www.nist.gov/srd/refprop>.
- [33] Menter FR. Review of the shear-stress transport turbulence model experience from an industrial perspective. *International Journal of Computational Fluid Dynamics*. 2009;23(4):305–316. Available from: <https://doi.org/10.1080/10618560902773387>.
- [34] Shah SR, Jain SV, Patel RN, Lakhera VJ. CFD for Centrifugal Pumps: A Review of the State-of-the-Art. *Procedia Engineering*. 2013;51:715–720. Available from: <https://www.sciencedirect.com/science/article/pii/S1877705813001033>.
- [35] Doustmohammadi A, Hajilouy Benisi A, Mojaddam M. Experimental and Numerical Investigation of Losses in Centrifugal Compressor Components. vol. 6; 2013.
- [36] Sundström E. Flow instabilities in centrifugal compressors at low mass flow rate; 2017.

A

Appendix 1

The plots of isentropic efficiency vs total pressure ratio and total pressure ratio vs volume flow rate are shown below. It can be observed that the range is longer than the one used as base case in the results chapter. The reason for this is that, the efficiency closer to the higher pressure ratio were not considered as they were suspected to be affected by numerical surge limit. For instance, it can be noted that the value of efficiency for the Star-CCM+ case in Figure A.2, at pressure ratio of approximately 1.4 is higher than the previous value of efficiency. This is physically not possible as the flow inside the compressor in this high pressure ratio region is extremely unstable and that it is basically avoided when using the compressor. Hence the results from these regions above pressure ratio of 1.4 were neglected as they might be misleading to the user that the compressor's efficiency is increasing. This can also be corroborated in the Figure A.1, where, for the volume flow rate of approximately 0.7 there are two different operating conditions or two pressure ratios seen which is not possible in reality.

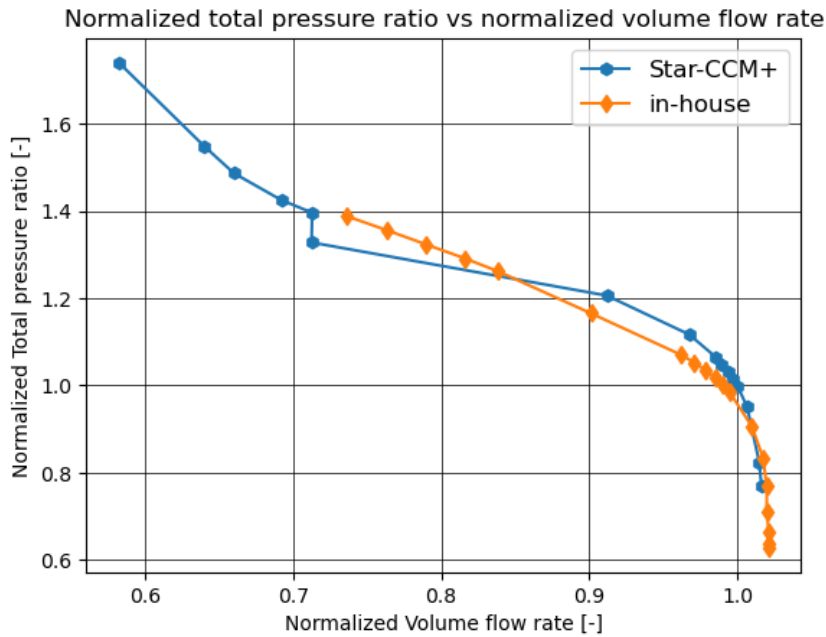


Figure A.1: Volume flow rate vs total pressure ratio plotted for the full range of simulation.

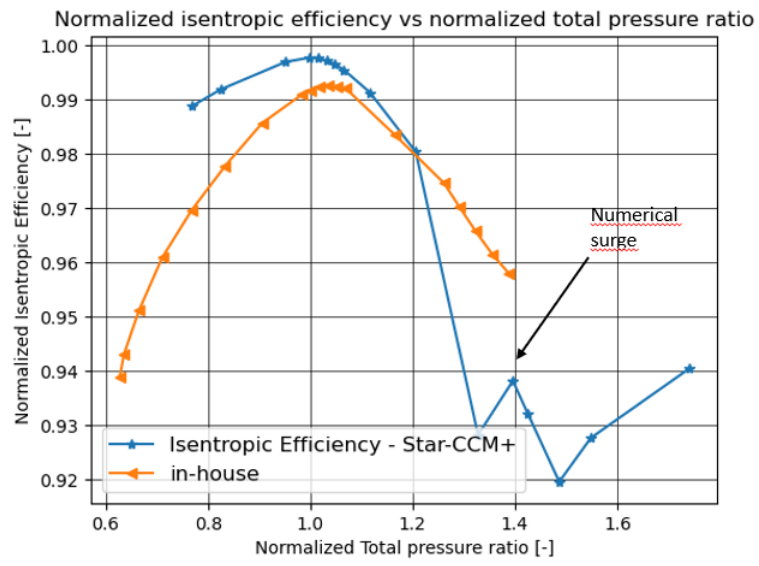


Figure A.2: Total pressure ratio vs isentropic efficiency plotted for the full range of simulation.

B

Appendix 2

In a CFD simulation, the residuals is one of the basic measure of a solution's convergence since it directly quantifies as the error in solution of system of equations. And since the residuals can never be zero in a simulation where the solution is attained through iterative process, the lower it is, the better as the solution attained will be numerically accurate.

Generally it is a good rule of thumb to have about 10^{-5} values of residuals to call a solution converged and it might not be attainable for all solutions but, never the less, it can be tried to be achieved through efficient meshing and setting the boundary conditions properly.

From the Figure B.1, B.2 and B.3, it can be seen that the residuals value vary when compared to each other and it is also noticed that the value of residuals are not below 10^{-5} for all the monitored variables in any of the simulation. Though it was tried to bring down the residuals by meshing with different strategies and applying different physics models, it did not work as expected. The reason could be due to the complex flow pattern faced by the fluid when flowing through the compressor and also since the fluid is getting compressed as it passes from the inlet to outlet, the physical and the numerical complexity increases. Combining that with the shock wave generated at the LE and TE of the impeller blades cause a significant discontinuity in the fluid properties and the environmental properties.

There is a difference between these figures because the operating conditions are distinctly different and hence have different effects on the flow. For example, when taking the case of Figure B.2, all the monitored values drop below residual value of 10^{-3} and remain almost constant with minor oscillations in the values. This might be due to the fact that this is the ideal operating conditions for the compressor and hence it is able to efficiently compress the fluid without generating additional losses. Though the same cannot be said for other two cases, hence the residual values are in the range of 10^{-1} and 10^{-2} . And the Figure B.1 is a bit better than the Figure B.3 as the flow/operating condition in the choke condition is better than the flow in a surge condition. Since the blades stall at low mass flow rates through the compressor, the mass imbalance through the compressor is not satisfied at all the locations due to the presence reversed flow, separated flow and other unwanted effects.

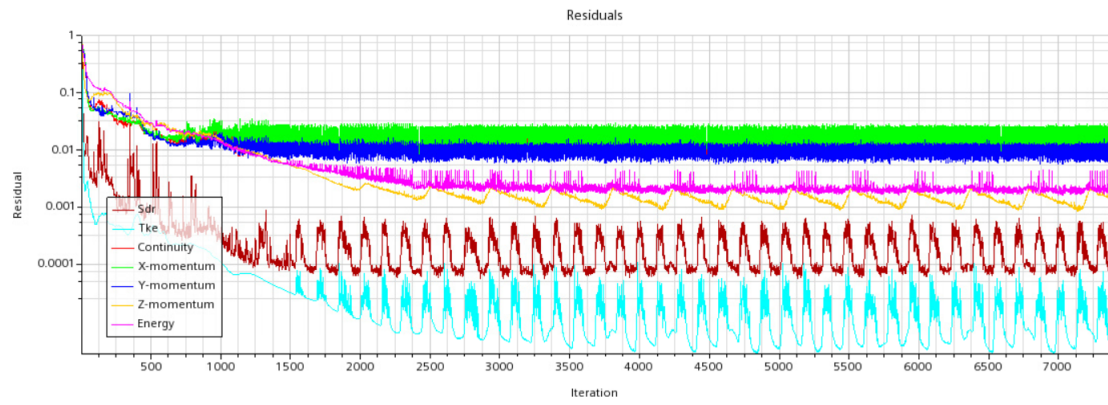


Figure B.1: Residuals - Choke region simulation.

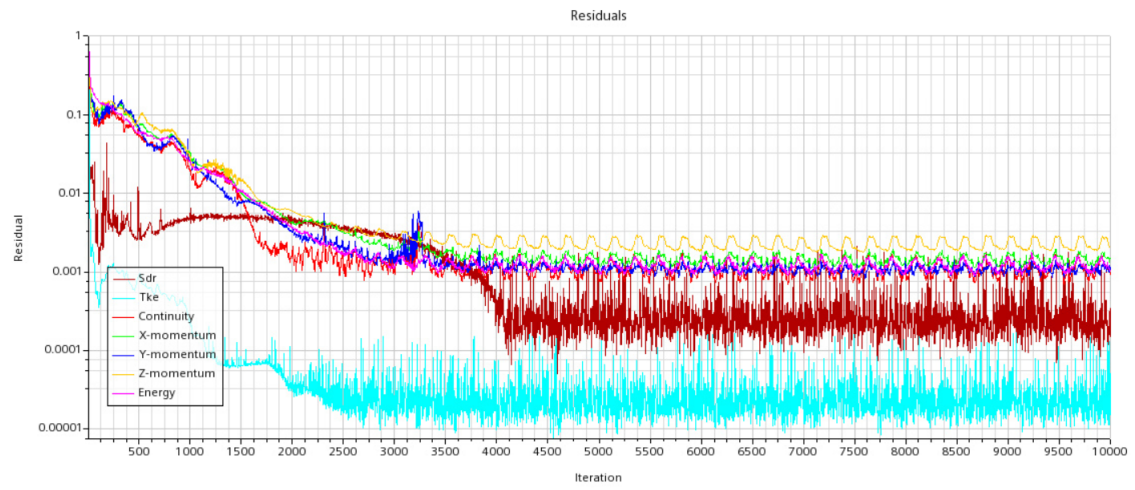


Figure B.2: Residuals - Design point region simulation.

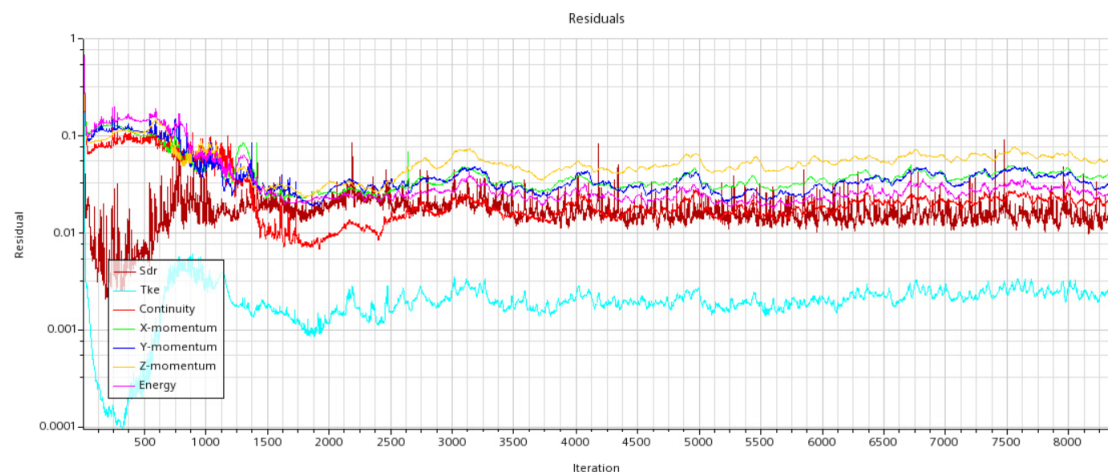


Figure B.3: Residuals - Surge region simulation.

C

Appendix 3

Here some extra contour plots of absolute Mach number and entropy for different spanwise locations and different operating conditions are shown, to give an idea about the difference between the relative mach number and the absolute one.

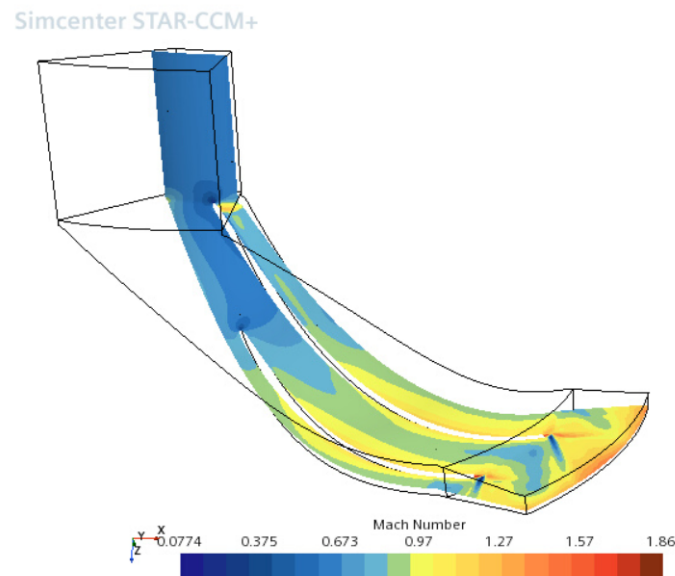


Figure C.1: Analysis of Mach number at the impeller and diffuser at 20% spanwise location for choking region operating condition.

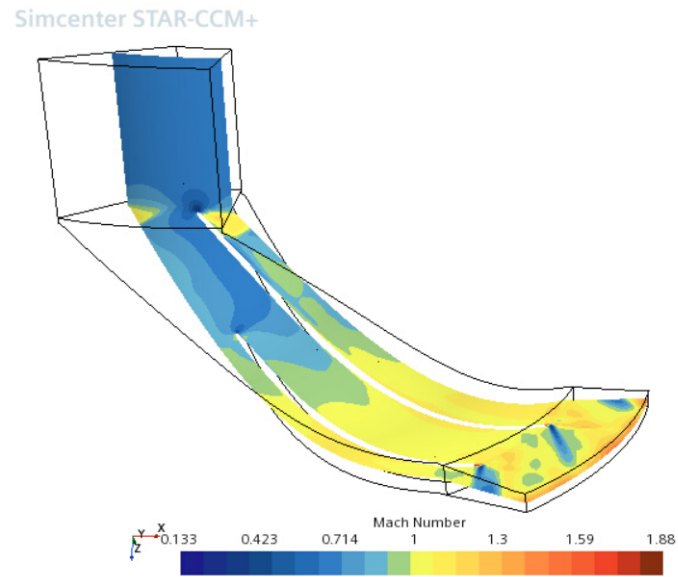


Figure C.2: Analysis of Mach number at the impeller and diffuser at 50% spanwise location for choking region operating condition.

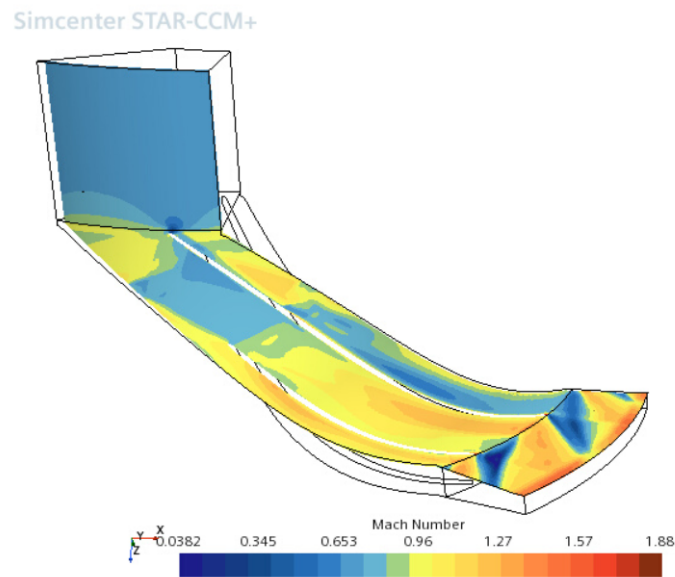


Figure C.3: Analysis of Mach number at the impeller and diffuser at 95% spanwise location for choking region operating condition.

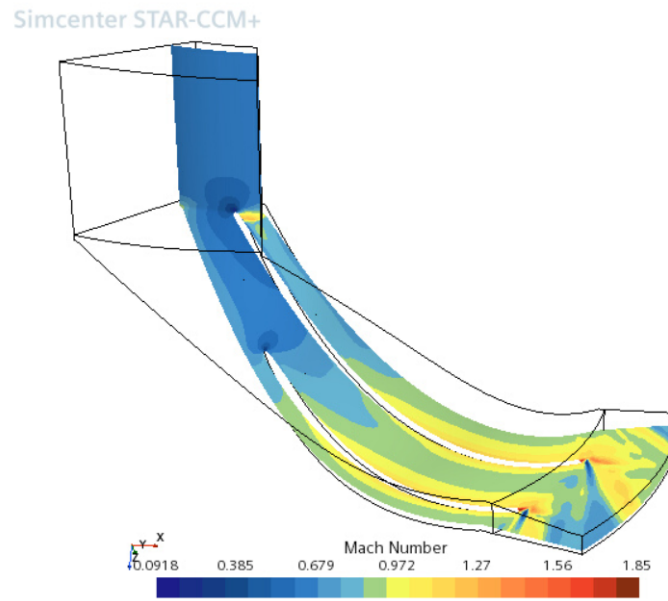


Figure C.4: Analysis of Mach number at the impeller and diffuser at 20% spanwise location for design point operating condition.

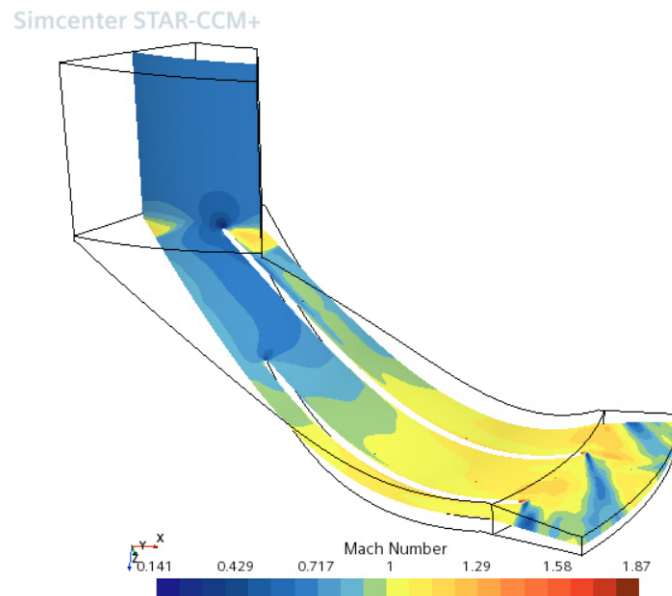


Figure C.5: Analysis of Mach number at the impeller and diffuser at 50% spanwise location for design point operating condition.

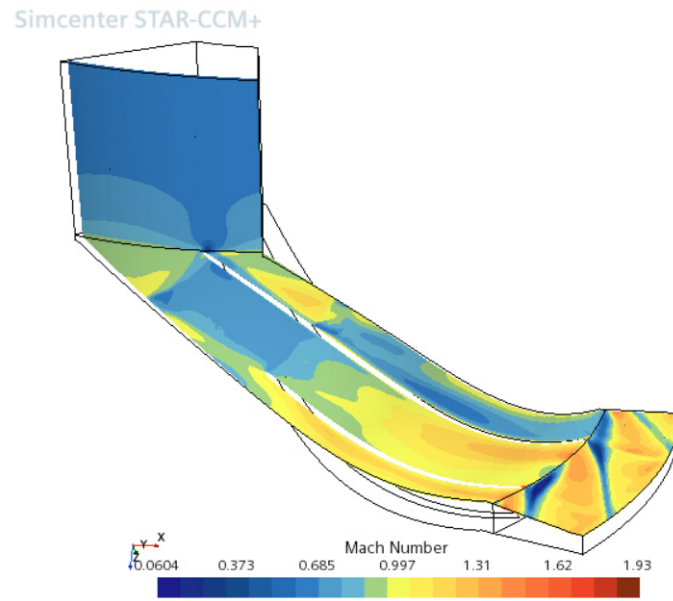


Figure C.6: Analysis of Mach number at the impeller and diffuser at 95% spanwise location for design point operating condition.

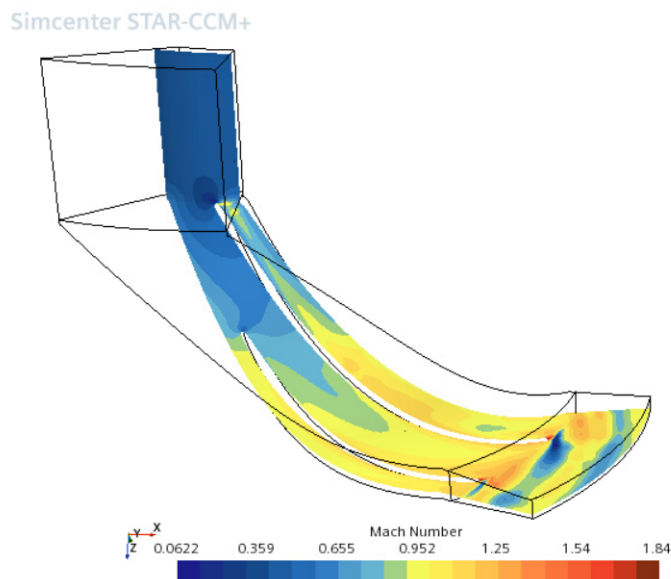


Figure C.7: Analysis of Mach number at the impeller and diffuser at 20% spanwise location for surge region operating condition.

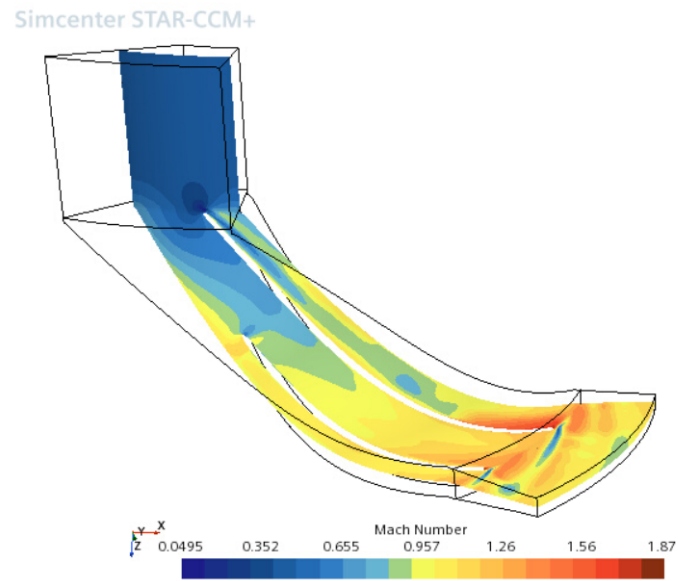


Figure C.8: Analysis of Mach number at the impeller and diffuser at 50% spanwise location for surge region operating condition.

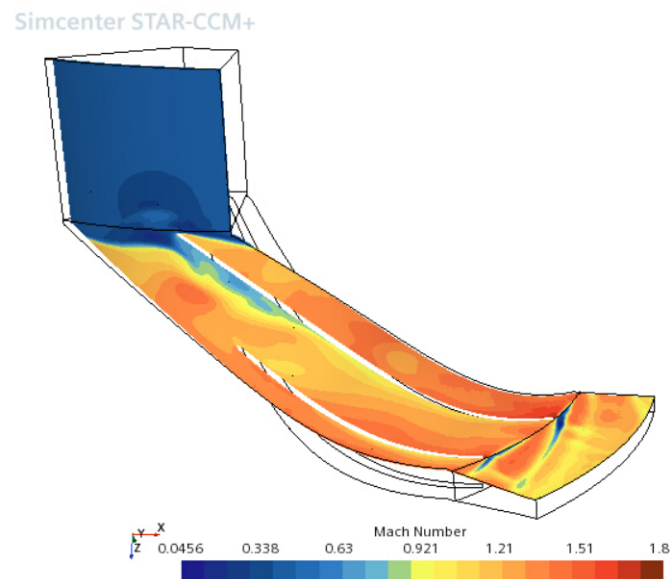


Figure C.9: Analysis of Mach number at the impeller and diffuser at 95% spanwise location for surge region operating condition.

The reason for displaying the entropy plots is that, they are main source behind the loss in a centrifugal compressor. Once generated the entropy does not exit the system but rather travels downstream and gets mixed into different regions much like smoke. Hence it is important to analyse the regions of high entropy.

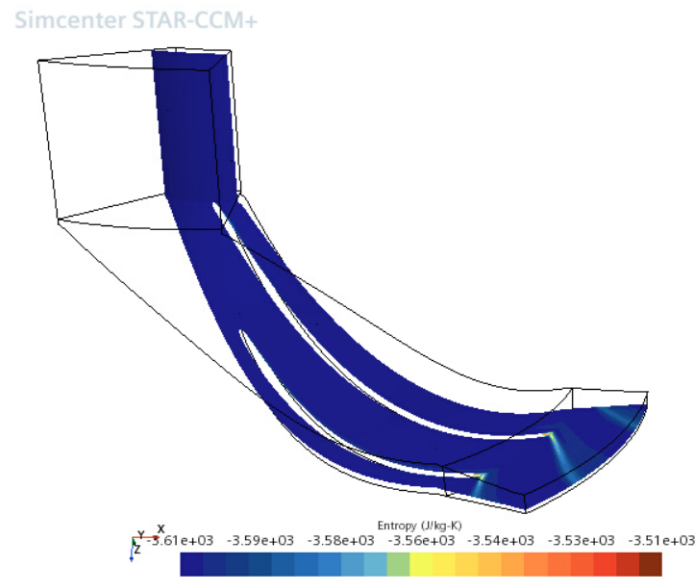


Figure C.10: Analysis of entropy at the impeller and diffuser at 20% spanwise location for choking region operating condition.

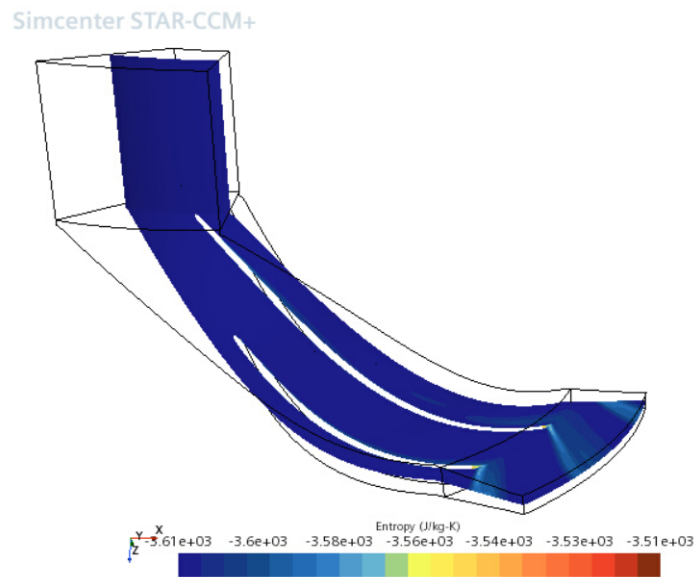


Figure C.11: Analysis of entropy at the impeller and diffuser at 50% spanwise location for choking region operating condition.

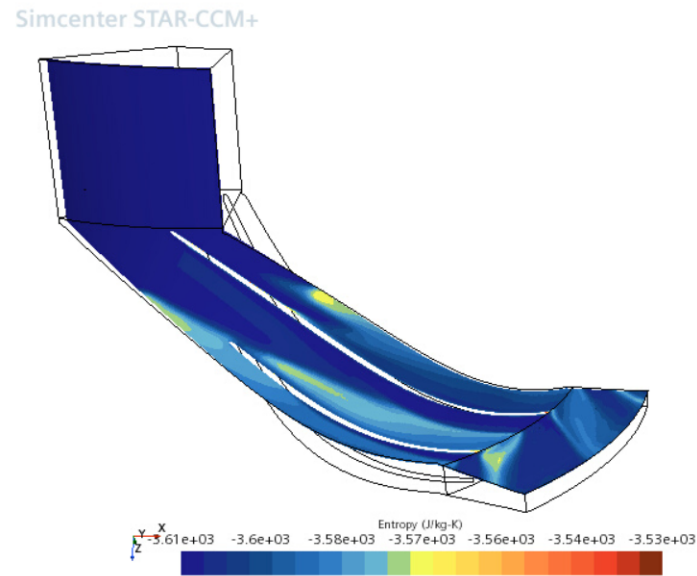


Figure C.12: Analysis of entropy at the impeller and diffuser at 95% spanwise location for choking region operating condition.

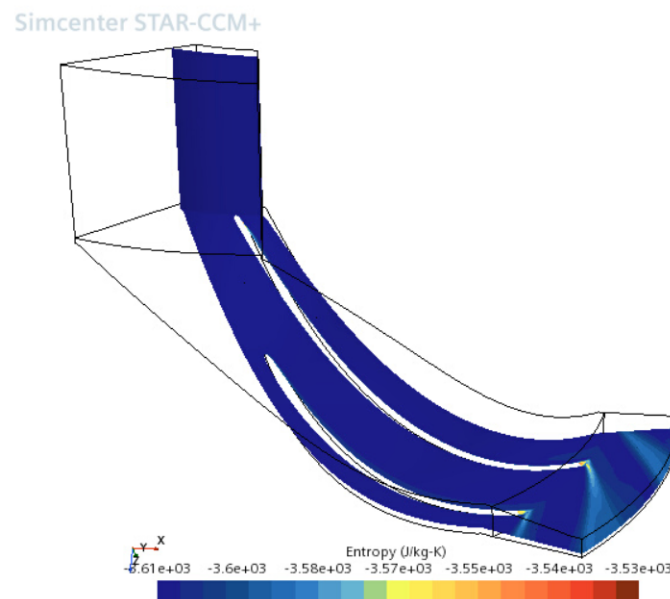


Figure C.13: Analysis of entropy at the impeller and diffuser at 20% spanwise location for design point operating condition.

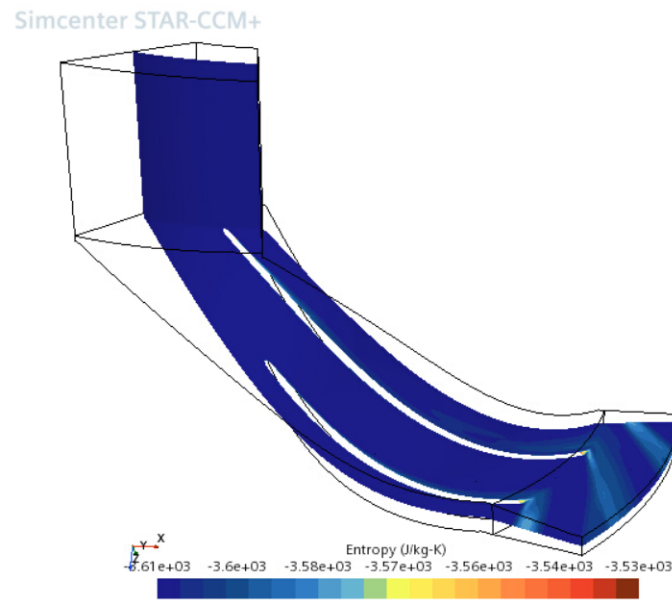


Figure C.14: Analysis of entropy at the impeller and diffuser at 50% spanwise location for design point operating condition.

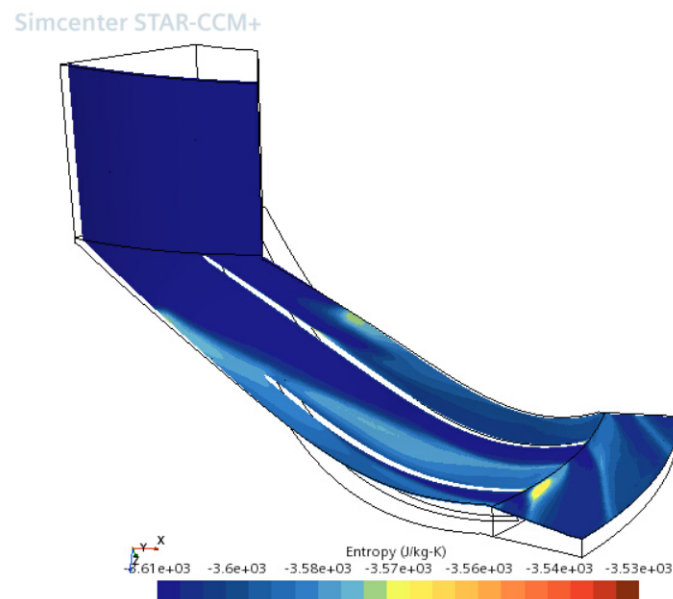


Figure C.15: Analysis of entropy at the impeller and diffuser at 95% spanwise location for design point operating condition.

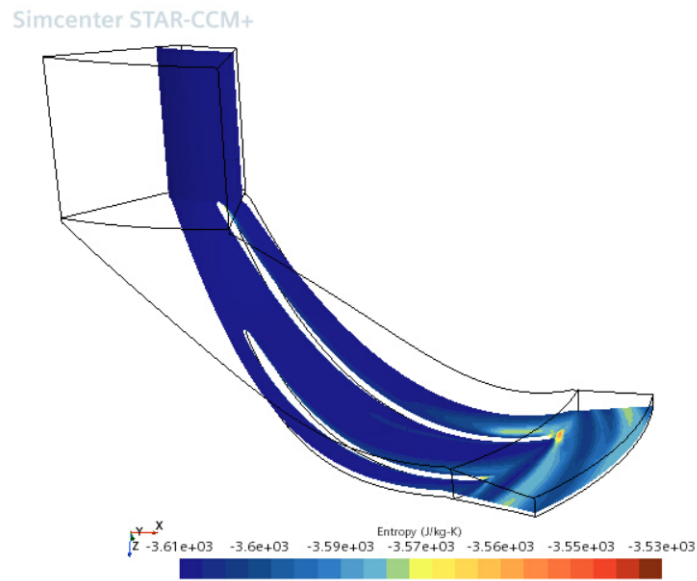


Figure C.16: Analysis of entropy at the impeller and diffuser at 20% spanwise location for surge region operating condition.

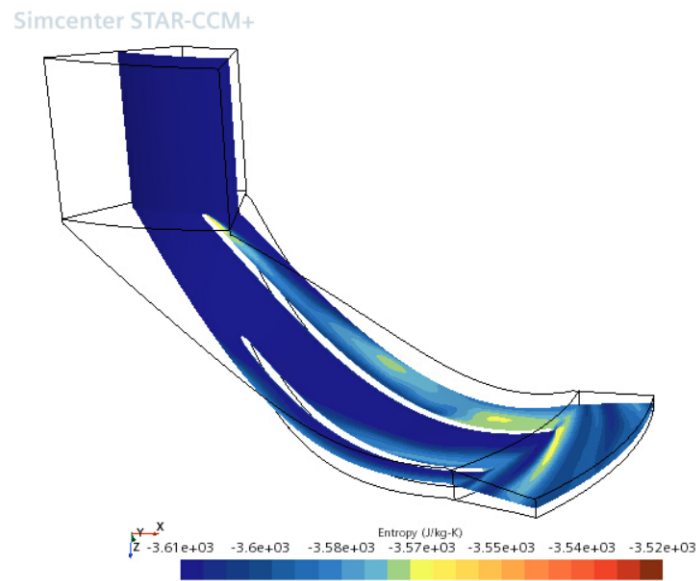


Figure C.17: Analysis of entropy at the impeller and diffuser at 50% spanwise location for surge region operating condition.

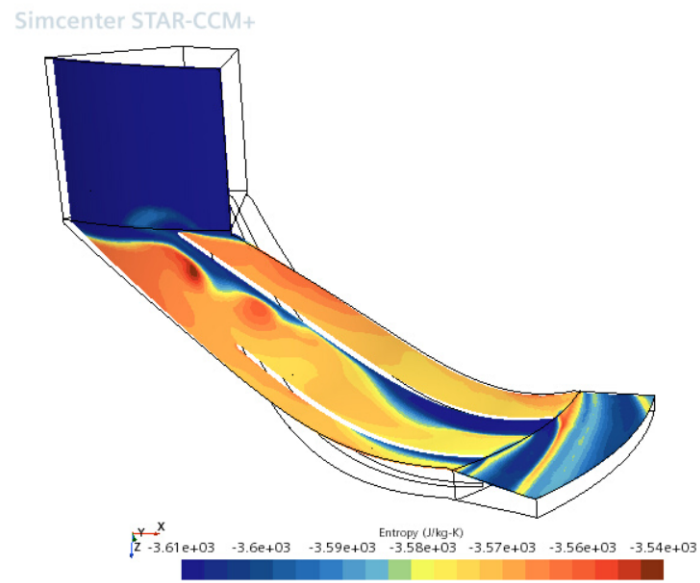


Figure C.18: Analysis of entropy at the impeller and diffuser at 95% spanwise location for surge region operating condition.

DEPARTMENT OF SOME SUBJECT OR TECHNOLOGY
CHALMERS UNIVERSITY OF TECHNOLOGY
Gothenburg, Sweden
www.chalmers.se



CHALMERS
UNIVERSITY OF TECHNOLOGY